ELSEVIER

Contents lists available at ScienceDirect

# Journal of Computational Physics

journal homepage: www.elsevier.com/locate/jcp



Numerical simulation and analysis of multiscale interface coupling between a poroelastic medium and a lumped hydraulic circuit: comparison between functional iteration and operator splitting methods

Lorena Bociu<sup>a</sup>, Giovanna Guidoboni<sup>b,\*</sup>, Riccardo Sacco<sup>c</sup>, Daniele Prada<sup>d</sup>

#### ARTICLE INFO

Article history:
Received XX
Received in final form XX
Accepted XX
Available online XX

Communicated by XX

multiscale interface coupling, poroelasticity, lumped hydraulic circuit, operator splitting, functional iterations

#### ABSTRACT

We consider a multiscale problem modeling the flow of a fluid through a deformable porous medium, described by a system of partial differential equations (PDEs), connected with a lumped hydraulic circuit, described by a system of ordinary differential equations (ODEs). This PDE/ODE coupled problem includes interface conditions enforcing the continuity of mass and the balance of stresses across models at different scales. In the present article, we address questions related to the solution methods of the PDE/ODE coupled problem via staggered algorithms, focusing on a detailed comparison between functional iterations and an energy-based operator splitting method and how they handle the interface conditions. We provide sufficient conditions for the convergence of functional iterations and prove that the energy-based operator splitting method is unconditionally stable with respect to the size of the time discretization step.

© 2022 Elsevier Inc. All rights reserved.

## 1. Introduction

Modeling of complex problems in science, engineering and medicine often requires the use of multiscale coupling between partial differential equations (PDEs) and ordinary differential equations (ODEs). The typical rationale is to provide an accurate three-dimensional (3D) description for a local region of interest, while simultaneously accounting for global features via a reduced lumped model. This multiscale strategy has been used successfully to study physiological flows, such as blood flow in the cardiovascular system or air flow in the respiratory tract [1, 2, 3, 4, 5, 6, 7, 8, 9, 10, 11, 12, 13, 14, 15, 16]. Particular attention has been devoted to the multiscale modeling of arterial blood flow, where Stokes or Navier-Stokes (S/NS) equations have been used as a 3D description for the

<sup>&</sup>lt;sup>a</sup>Department of Mathematics, North Carolina State University, Raleigh, NC, 27695, USA

<sup>&</sup>lt;sup>b</sup>Department of Electrical Engineering and Computer Science, Department of Mathematics, University of Missouri, Columbia, MO, 65211, USA

<sup>&</sup>lt;sup>c</sup>Dipartimento di Matematica, Politecnico di Milano, Milano, 20133, Italy

<sup>&</sup>lt;sup>d</sup>Istituto di Matematica Applicata e Tecnologie Informatiche "Enrico Magenes", Consiglio Nazionale delle Ricerche, Pavia, 27100, Italy

<sup>\*</sup>Corresponding author:

blood flow through a main artery while accounting for the rest of the circulation via zero-dimensional (0D) lumped models in which the only independent variable is time [8, 9, 10, 11, 12, 13, 14, 15, 16]. The coupling between a 3D Biot system and one-dimensional (1D) flow equations has also been considered with application in biology and geosciences [17, 18, 19, 20, 21, 22, 23].

Our paper is focused on biological models where the perfusion of a tissue, which is a local phenomenon, is studied in correlation with the global features of the surrounding blood circulation. Our work is motivated by the fact that many pathologies are related to hemodynamic changes occurring at the microvascular level, where small vessels pierce the tissue perfusing it with blood. Due to the small caliber and large number of such vessels, it is impractical to model each one of them separately via S/NS equations as is traditionally done for large arteries. To address this issue, deformable porous media models have been proposed for tissue perfusion, where blood vessels are modeled as pores within a deformable solid representing the tissue [24, 25, 26, 27, 28, 29]. While studies for deformable porous media in biological models are available [25, 26, 27, 30, 31, 32, 33], their coupling with 0D lumped models accounting for systemic features has yet to be tackled and brings new challenges that constitute the main focus of this work.

Specifically, we consider a multiscale model where a PDE description of tissue perfusion, based on deformable porous media, is coupled with an ODE description of the blood circulation to and from the tissue of interest, based on the analogy between fluid flows and electrical circuits (Sections 2 and 3). This multiscale problem includes interface conditions enforcing the continuity of mass and the balance of stresses across models at different scales, so that the resulting system involves linear PDEs of mixed type, with interface conditions depending on ODEs. In the present article, we address questions related to solution methods based on staggered algorithms of the multiscale problem described above, focusing on a detailed comparison between functional iterations and an energy-based operator splitting method and how they "handle" the interface conditions (Section 4). After setting the problem in its general 3D-0D formulation, we present a specific example where a 1D version of the Biot problem is coupled with a 0D lumped circuit (Section 5). This example yields an analytic solution (Appendix) and enables a thorough comparison between the techniques of functional iterations and operator splitting. Furthermore, we provide sufficient conditions for the convergence of functional iterations when applied to the 1D-0D example by means of a Backward Euler time-discretization, and we prove unconditional stability for the energy-based operator splitting method with respect to the size of the time discretization step (Section 6). Unconditional stability of the operator splitting method is a consequence of the fact that the splitting step does not disrupt the energy balance holding at the continuous level, ensuring in particular that the dissipation mechanism has a nonnegative sign. Based on this consideration, we investigate how dissipation is handled by the method based on functional iterations and its connection with failure of convergence (Section 7). In addition to the solution of 1D-0D coupled problems, simulations are also presented for the full 3D-0D case. The numerical results support the theoretical findings and, interestingly, confirm that decreasing the time step size does not always guarantee convergence for the functional iterations (Section 8). Conclusions and future developments of the solution algorithms analyzed in this work are illustrated in Section 9.

#### 2. Mathematical formulation

Let us consider a poroelastic Biot model (see [34]) in the spatial domain  $\Omega \subset \mathbb{R}^3$  connected to a lumped hydraulic circuit  $\Upsilon$ , as shown in Fig. 1. The circuit  $\Upsilon$  comprises an internal part  $\widetilde{\Upsilon}$  that is not directly connected to the Biot model and a connecting part  $\Lambda$ . In this work,  $\Lambda$  represents a compliant hydraulic buffer, whose electric representation consists of a linear time-invariant resistor R and a linear time-invariant capacitor C, as often encountered in blood flow models [12, 35, 36]. The Biot-circuit connection occurs at the interface  $\Sigma$ , which constitutes part of the boundary of  $\Omega$ . The remaining part of the boundary is denoted by  $\Gamma$ , so that we can write  $\partial\Omega = \Gamma \cup \Sigma$ . The differential problems describing the poroelastic Biot model and the lumped hydraulic circuit are detailed in Sections 2.1 and 2.2, respectively. Boundary, interface and initial conditions are illustrated in Section 2.3.

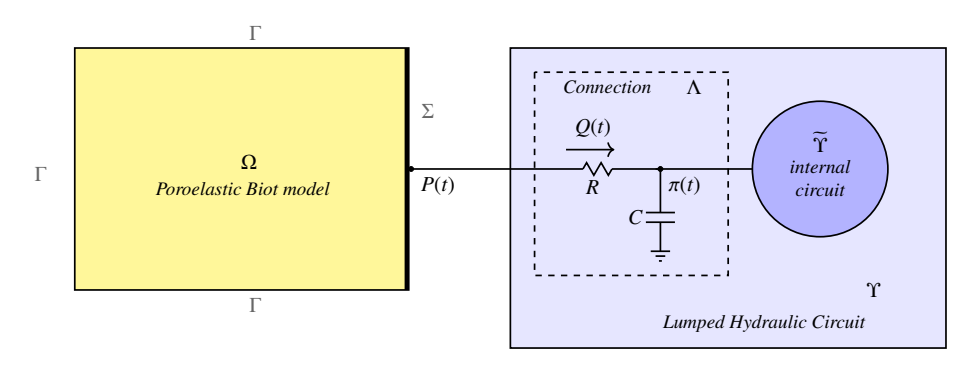


Fig. 1: The Biot region  $\Omega$  is connected to the lumped circuit  $\Upsilon$ . The connection  $\Lambda$  represents a compliant hydraulic buffer, whose electric representation consists of a linear time-invariant resistor R and a linear time-invariant capacitor C. The internal circuit  $\widetilde{\Upsilon}$  contains all the lumped elements that are not directly connected to the interface  $\Sigma$ .

#### 2.1. Poroelastic Biot model

We consider a poroelastic Biot model with incompressible components described by the following PDE system:

$$\frac{\partial \zeta}{\partial t} + \nabla \cdot \mathbf{v} = S \qquad \qquad \text{in } \Omega \times (0, T), \tag{1a}$$

$$\nabla \cdot \mathbf{T} + \mathbf{f} = \mathbf{0} \qquad \qquad \text{in } \Omega \times (0, T), \tag{1b}$$

$$\zeta = \phi - \phi_0 \qquad \text{in } \Omega \times (0, T), \tag{1c}$$

$$\phi = \nabla \cdot \boldsymbol{u} + \phi_0 \qquad \qquad \text{in } \Omega \times (0, T), \tag{1d}$$

$$\mathbf{v} = -k\nabla p,$$
 in  $\Omega \times (0, T),$  (1e)

$$\mathbf{T} = 2\mu \mathbf{E}(\mathbf{u}) + \lambda \operatorname{tr}(\mathbf{E}(\mathbf{u}))\mathbf{I} - p\mathbf{I} \qquad \text{in } \Omega \times (0, T), \tag{1f}$$

where  $\Omega \subset \mathbb{R}^3$  is a bounded spatial domain and (0,T) is a time interval. Eq. (1a) represents the balance of mass of the fluid phase, Eq. (1b) represents the balance of momentum for the whole mixture and Eqs. (1c)-(1f) represent the constitutive equations that are necessary to close the system. The unknowns of the problem are the fluid content  $\zeta$  (unitless), the discharge (or Darcy) velocity v (units: ms<sup>-1</sup>), the stress tensor  $\mathbf{T}$  (units: Nm<sup>-2</sup>), the porosity  $\phi$  (unitless), the displacement  $\mathbf{u}$  (units: m) and the pressure p (units: Nm<sup>-2</sup>). The tensor  $\mathbf{E}(\mathbf{w})$  is the symmetric part of the gradient of the vector field  $\mathbf{w}$  defined as

$$\mathbf{E}(\mathbf{w}) = \frac{1}{2} (\nabla \mathbf{w} + (\nabla \mathbf{w})^T)$$

and  $\operatorname{tr}(\mathbf{E}(w))$  is the trace of the tensor  $\mathbf{E}(w)$ . We emphasize that all the aforementioned variables are functions of both space and time. In particular, we have u=u(x,t) and p=p(x,t), for  $x\in\Omega$  and  $t\in(0,T)$ , from which it follows that  $\phi=\phi(u(x,t)),\ \zeta=\zeta(u(x,t)),\ v=v(p(x,t))$  and  $\mathbf{T}=\mathbf{T}(u(x,t),(p(x,t)))$ . The model also includes volumetric sources of fluid content and linear momentum, denoted by S=S(x,t) (units:  $s^{-1}$ ) and f=f(x,t) (units:  $s^{-1}$ ), respectively. The model parameters are the reference porosity  $\phi_0$  (unitless), the permeability k (units:  $s^{-1}$ ), and the elastic Lamé parameters  $\mu$  and  $\lambda$  (units:  $s^{-1}$ ), which are assumed to be given positive constants.

We note that the poroelastic model described by the PDE system (1) assumes that both fluid and solid components are incompressible, the mechanic behavior is stress free, linearly elastic and isotropic, and the distribution of pores within the medium is isotropic. Volumetric sources of mass within the medium may represent injections of fluid which, in turn, may give rise to volumetric sources of linear momentum [34, 37, 38, 24]. Potential extensions of the model motivated by applications in biology and bioengineering include: tissue viscoelasticity, compressibility and anisotropy [37, 29]; tissue growth and remodeling [39, 40]; mass balance of cellular components [41, 42]; electroosmotic fluid pressure gradients [43, 44]. Gravitational effects may also be important and they will affect both the Darcy law and the volumetric sources of linear momentum [45]. We remark that this work focuses on staggered approaches for the solution methods of the coupling between the poroelastic problem and the lumped circuit so that, thanks to the modularity of the resulting algorithms, potential extensions of the poroelastic model will be limited to the pertaining module and, as a consequence, easier to include.

#### 2.2. Lumped circuit

In the lumped circuit, the fluid flow through an hydraulic network is described via its analogy with a current flowing through an electric circuit, where active sources of voltage and current represent pressure and flow rate sources, whereas passive elements such as resistances, inductances and capacitances, represent viscous effects, inertial effects and vessel compliance, respectively [24]. For the sake of simplicity, in this work we consider linear time-invariant resistors, capacitors and inductors, even though the approach could be extended to the more general case of nonlinear time-varying elements. In hydraulic terms, this means that we are assuming the vasculature to be compliant, but with small deformations, and passive. Potential extensions motivated by biological applications include large deformations, such as those associated with vein collapsibility, and active changes in vessel diameters and biomechanical properties, such as those due to regulatory mechanisms [46]. We remark that, in the spirit of staggered algorithms, potential extensions of the lumped circuit model will affect its module within the whole algorithm, thereby making them easier to include.

Specifically, let us assume that the internal circuit  $\widetilde{\Upsilon}$  includes  $n_R$  resistors with constant resistances  $R_i > 0, i = 1, \dots, n_R, n_C$  capacitors with constant capacitances  $C_i > 0, i = 1, \dots, n_C$ , and  $n_L$  inductors with constant inductances  $L_i > 0, i = 1, \dots, n_L$ . Furthermore, we assume that the connection  $\Lambda$  consists of a resistor of resistance R and a capacitor of capacitance C connected to the ground, where zero pressure is assumed.

Following [47], we introduce a vector y(t) of state variables characterizing the circuit  $\Upsilon$ , where state variables are associated with each capacitor and inductor. The connection  $\Lambda$  includes a single capacitor connected to the ground, so that the appropriate state variable is the pressure  $\pi(t)$  (units: Nm<sup>-2</sup>) at the connecting node, as indicated in Fig. 1. The internal circuit  $\Upsilon$  includes multiple inductors and capacitors, so that the appropriate state variables are the volumetric flow rate Q(t) (units: m<sup>3</sup>s<sup>-1</sup>) across each inductor and the pressure difference  $\Pi(t)$  (units: Nm<sup>-2</sup>) across each capacitor, so that we can define the vector  $\widetilde{y}(t)$  of state variables characterizing  $\Upsilon$  as follows

$$\widetilde{\mathbf{y}}(t) = [\Pi_1(t), \dots, \Pi_{n_C}(t), Q_1(t), \dots, Q_{n_L}(t)]^T.$$
 (2)

Finally, we can define the vector of state variables y(t) for the whole circuit  $\Upsilon$  as follows

$$\mathbf{y}(t) = \begin{bmatrix} \pi(t) \\ \widetilde{\mathbf{y}}(t) \end{bmatrix} \tag{3}$$

where  $y(t) \in \mathbb{R}^d$  and  $d = 1 + n_C + n_L$ . The dynamics of  $\Upsilon$  is described by the following ODE system:

$$\frac{d\mathbf{y}(t)}{dt} = \mathbf{A}\mathbf{y}(t) + \mathbf{s}(t) + \mathbf{b}(Q(t)) \qquad \text{in } (0, T).$$
 (4)

The  $d \times d$  matrix **A** has given constant entries that depend on the circuit graph and on the values of the resistances, capacitances and inductances within the circuit. The  $d \times 1$  vector s(t) represents the sources of voltage and current present in  $\widetilde{\Upsilon}$ . The  $d \times 1$  vector b(Q(t)) represents the contribution from the connection with the poroelastic Biot model and can be written as

$$\boldsymbol{b}(Q(t)) = \frac{Q(t)}{C} \boldsymbol{e}_1 \quad \text{with} \quad \boldsymbol{e}_1 = [1, \ \mathbf{0}]^T$$
 (5)

where Q = Q(t) is the volumetric flow rate through the connecting resistor, as shown in Fig. 1, and  $\mathbf{0} \in \mathbb{R}^{1 \times (d-1)}$ .

#### 2.3. Boundary, interface and initial conditions

The poroelastic Biot model (1) can be completed with different boundary conditions representing different physical constraints on the portion  $\Gamma$  of  $\Omega$ . Specifically, let us write  $\Gamma = \Gamma_{D,v} \cup \Gamma_{D,p} \cup \Gamma_N \cup \Gamma_0$  and let us assume that the following boundary conditions are imposed:

$$\mathbf{T} \, \boldsymbol{n} = \boldsymbol{g}, \qquad \qquad \boldsymbol{v} \cdot \boldsymbol{n} = 0, \qquad \qquad \text{on } \Gamma_N \times (0, T), \tag{6a}$$

$$\boldsymbol{u} = \boldsymbol{0}, \qquad p = 0, \qquad \text{on } \Gamma_{D,p} \times (0,T),$$
 (6b)

$$\boldsymbol{u} = \boldsymbol{0}, \qquad \boldsymbol{v} \cdot \boldsymbol{n} = \psi, \qquad \text{on } \Gamma_{D,v} \times (0,T),$$
 (6c)

$$(\mathbf{T} \mathbf{n}) \cdot \boldsymbol{\tau}_1 = 0, \qquad (\mathbf{T} \mathbf{n}) \cdot \boldsymbol{\tau}_2 = 0, \qquad \text{on } \Gamma_0 \times (0, T), \tag{6d}$$

$$\boldsymbol{u} \cdot \boldsymbol{n} = 0,$$
  $\boldsymbol{v} \cdot \boldsymbol{n} = 0,$  on  $\Gamma_0 \times (0, T),$  (6e)

where g and  $\psi$  are given functions of space and time, n is the outward unit normal vector to the surface  $\partial\Omega$ , and  $\tau_i$ , with i = 1, 2, are the tangential unit vectors to the surface. We remark that conditions (6a)-(6c) are the same as those considered in [31], whereas conditions (6d)-(6e) are instrumental for the derivation of the 1D model illustrated in Section 5. On the interface  $\Sigma$ , we impose the following conditions:

$$\boldsymbol{u}(\boldsymbol{x},t) = \boldsymbol{0},\tag{7a}$$

$$\int_{\Sigma} \mathbf{v}(\mathbf{x}, t) \cdot \mathbf{n}(\mathbf{x}) \, d\mathbf{x} = Q(t), \tag{7b}$$

$$p(\mathbf{x},t) = P(t),\tag{7c}$$

holding for  $x \in \Sigma$ ,  $t \in \times (0, T)$ . By applying the hydraulic analog to Ohm's law, namely Poiseuille's law, to the resistor in  $\Lambda$  that connects the poroelastic Biot model with the lumped circuit, we can write

$$Q(t) = \frac{P(t) - \pi(t)}{R} \tag{8}$$

where P(t) and  $\pi(t)$  are the pressures at the Biot and circuit ends of the resistor, as shown in Fig. 1.

Finally, we prescribe the following initial conditions:

$$u(x,0) = \chi(x)$$
 for  $x \in \Omega$  (9a)

$$\mathbf{y}(0) = \mathbf{y}_0 \tag{9b}$$

with  $\chi(x)$  and  $y_0$  given.

Coupled Problem. The fully coupled problem consists in finding u, p, y, P, Q that satisfy equations (1) and (4), subject to the interface conditions (7) - (8), boundary conditions (6) and initial conditions (9). Existence of solutions to the fully coupled problem is an open question in the field. The PDE system is the linear quasi-static Biot model with incompressible constituents. There are many well-posedness results available in the literature regarding well-posedness for poro-elastic systems, both in linear [48, 49, 50] and nonlinear scenarios (where the permeability is a nonlinear function of pressure or solid dilation) [51, 52, 31, 53, 54]. In comparison, the Biot problem considered in this article is different, since boundary conditions are not prescribed on  $\Sigma$ , but instead we have interface conditions that couple the poroelastic domain with the circuit. In particular, the PDE/ODE coupling involves nonlocal interface conditions enforcing the continuity of mass and the balance of stresses across different scales. Notably, even though similar nonlocal interface conditions arise in 3D/0D models involving the Stokes/Navier Stokes equations [1, 4, 9, 10, 11, 14], the mathematical challenges that these conditions bring for deformable porous media are very different. Unlike the Stokes/Navier-Stokes case, in deformable porous media the discharge velocity is not solenoidal, thereby yielding less control over its normal component at the interface, whose integral appears in the interface conditions. This difference calls for novel theoretical and computational approaches. The latter part is what we address in this paper.

# 3. Energy identity for the fully coupled problem

The mathematical problem illustrated in Section 2 is characterized by an energy identity that captures the physical phenomena governing the dynamics of the coupled system. Thus, when devising a numerical method for the solution of the problem, it should be verified whether and to what extent such energy identity still holds at the discrete level. This important aspect is examined in Section 6 in the case of the Operator Splitting method and in Section 7 in the case of the PQP and QPQ functional iterations.

In order to obtain the energy identity, we begin by focusing on the Biot problem. Let  $u_t$  denote the partial derivative of u(x, t) with respect to t. Using multipliers p and  $u_t$  for the mass balance equation and the linear momentum balance equation, respectively, and recalling the boundary and interface conditions, we obtain

$$\frac{d}{dt}\mathcal{E}_{\Omega}(\boldsymbol{u}) + \mathcal{D}_{\Omega}(\boldsymbol{p}) = \mathcal{F}_{\Omega}(\boldsymbol{f}, \boldsymbol{S}; \boldsymbol{u}, \boldsymbol{p}) + \mathcal{F}_{\partial\Omega}(\boldsymbol{g}, \boldsymbol{\psi}; \boldsymbol{u}, \boldsymbol{p}) - P(t)Q(t)$$
(10)

where the elastic energy  $\mathcal{E}_{\Omega}(\boldsymbol{u})$ , the viscous dissipation  $\mathcal{D}_{\Omega}(p)$  and the forcing terms  $\mathcal{F}_{\Omega}(\boldsymbol{f}, S; \boldsymbol{u}, p)$  and  $\mathcal{F}_{\partial\Omega}(\boldsymbol{g}, \psi; \boldsymbol{u}, p)$  are given by:

$$\mathcal{E}_{\Omega}(\boldsymbol{u}) = \frac{\lambda}{2} \|\nabla \cdot \boldsymbol{u}\|_{L^{2}(\Omega)}^{2} + \mu \|\mathbf{E}(\boldsymbol{u})\|_{L^{2}(\Omega)}^{2}$$
(11)

$$\mathcal{D}_{\Omega}(p) = \|k^{1/2} \nabla p\|_{L^2(\Omega)}^2 \tag{12}$$

$$\mathcal{F}_{\Omega}(f, S; \boldsymbol{u}, p) = \int_{\Omega} f \cdot \boldsymbol{u}_t \, d\Omega + \int_{\Omega} S \, p \, d\Omega \tag{13}$$

$$\mathcal{F}_{\partial\Omega}(\boldsymbol{g}, \boldsymbol{\psi}; \boldsymbol{u}, p) = \int_{\Gamma_N} \boldsymbol{g} \cdot \boldsymbol{u}_t \, d\Gamma_N - \int_{\Gamma_{D,v}} \psi p \, d\Gamma_{D,v} \,. \tag{14}$$

Then we consider the ODE system describing the dynamics of the circuit. We define the following diagonal matrix whose positive entries are given by the capacitances and inductances present in the lumped circuit

$$\mathbf{U} := \operatorname{diag}([C, C_1, \dots, C_{n_C}, L_1, \dots, L_{n_L}]). \tag{15}$$

Using multiplier Uy in system (4), we obtain the following identity

$$\frac{d\mathcal{E}_{\Upsilon}(\mathbf{y})}{dt} + \mathcal{D}_{\Upsilon}(\mathbf{y}) = \mathcal{F}_{\Upsilon}(\mathbf{s}; \mathbf{y}) + (\mathbf{U}\mathbf{y}) \cdot \boldsymbol{b}(Q(t)), \tag{16}$$

where  $\mathcal{E}_{\Upsilon}(y)$  and  $\mathcal{D}_{\Upsilon}(y)$  are defined as:

$$\mathcal{E}_{\Upsilon}(\mathbf{y}) = \frac{C\pi^2}{2} + \sum_{i=1}^{n_C} \frac{C_i \Pi_i^2}{2} + \sum_{i=1}^{n_L} \frac{L_i Q_i^2}{2}$$
 (17)

$$\mathcal{D}_{\Upsilon}(\mathbf{y}) = (\mathbf{B}\mathbf{y}) \cdot \mathbf{y} \tag{18}$$

$$\mathcal{F}_{\Upsilon}(s; \mathbf{y}) = (\mathbf{U}\mathbf{y}) \cdot \mathbf{s} \tag{19}$$

 $\mathcal{E}_{\Upsilon}(\mathbf{y})$  being the energy stored in the capacitors and inductors within the circuit  $\Upsilon$ . The matrix **B** is given by

$$\mathbf{B} = -\mathbf{U}\,\mathbf{A}.\tag{20}$$

Since we are considering linear time-invariant elements, the circuit is passive and, consequently, the matrix **B** is positive definite [47], thereby attributing to the functional  $\mathcal{D}(y)$  the meaning of a dissipation of energy within the circuit elements. Lastly,  $\mathcal{F}_{\Upsilon}(s;y)$  represents the forcing on the system due to sources of flow rate and pressure (analogous to current and voltage sources) within the circuit. Now, using the definition (15) of the matrix **U** and the definition (5) of the vector  $\boldsymbol{b}$ , we obtain that

$$(\mathbf{U}\mathbf{y}) \cdot \mathbf{b}(Q(t)) = \pi(t)Q(t)$$

and therefore (16) becomes

$$\frac{d\mathcal{E}_{\Upsilon}(\mathbf{y})}{dt} + \mathcal{D}_{\Upsilon}(\mathbf{y}) = \mathcal{F}_{\Upsilon}(\mathbf{s}; \mathbf{y}) + \pi(t)Q(t). \tag{21}$$

Combining (10) and (21) we obtain

$$\frac{d}{dt} \left( \mathcal{E}_{\Omega}(\boldsymbol{u}) \right) + \mathcal{E}_{\Upsilon}(\boldsymbol{y}) + \mathcal{D}_{\Omega}(p) + \mathcal{D}_{\Upsilon}(\boldsymbol{y}) = \tag{22}$$

$$\mathcal{F}_{\Omega}(f, S; \boldsymbol{u}, p) + \mathcal{F}_{\partial\Omega}(g, \psi; \boldsymbol{u}, p) + \mathcal{F}_{\Upsilon}(s; \boldsymbol{y}) + Q(t)(\pi(t) - P(t)).$$

Finally, using (8) in (22), we obtain the following energy identity for the fully coupled system

$$\frac{d}{dt}\left(\mathcal{E}_{\Omega}(\boldsymbol{u})\right) + \mathcal{E}_{\Upsilon}(\boldsymbol{y}) + \mathcal{D}_{\Omega}(p) + \mathcal{D}_{\Upsilon}(\boldsymbol{y}) + \mathcal{D}_{\Lambda}(Q)$$
(23)

$$= \mathcal{F}_{\Omega}(\mathbf{f}, S; \mathbf{u}, p) + \mathcal{F}_{\partial\Omega}(\mathbf{g}, \psi; \mathbf{u}, p) + \mathcal{F}_{\Upsilon}(\mathbf{s}; \mathbf{y})$$

where

$$\mathcal{D}_{\Lambda}(Q) = RQ^2(t) \tag{24}$$

is the dissipation due to the resistive connection between the Biot region and the internal circuit. It is interesting to remark that the non-negativity of the term in (24) is a direct consequence of the positivity of R and the physics of the multiscale interface where the conservation of mass and the continuity of pressure must hold.

**Remark 1.** Besides its physical importance within the energy balance of the system at hand, the dissipation term (24) is also relevant in affecting the stability and convergence properties of the solution methods employed for the numerical approximation of the coupled Biot-circuit problem. This critical aspect is analyzed theoretically (see Sections 6 and 7) and investigated numerically (see Section 8) for the staggered algorithms considered in this work (see Section 4).

#### 4. Solution methods

In this work, we consider and compare two main staggered approaches for the solution of the coupled problem illustrated in Section 2. The two approaches are described at the continuous level as far as the spatial variable is concerned, whereas the time interval is divided into a partition of finite size. The two approaches are then numerically approximated in time using the Backward Euler method and in space using the Finite Element Method as described in Section 8. The first approach is based on functional iterations (see Section 4.1), also referred to as fixed-point iterations or Picard iterations, see [55], whereas the second approach is based on operator splitting (see Section 4.2). Both approaches are modular and address the need of solving in separate substeps the PDE system associated with the Biot model and the ODE system associated with the lumped circuit, so that potential extensions motivated by particular applications can be dealt with in the corresponding module. However, the way in which this decoupling is achieved makes the two approaches very different. Particular attention will be devoted to the treatment of the interface conditions (7b), (7c) and (8), which also play a crucial role in ensuring the non-negativity of the term  $\mathcal{D}_{\Lambda}(Q)$  in the energy identity (22) for the full coupled system at the continuous level.

For the sake of simplicity, we consider a uniform partition of the time interval [0, T], with  $\Delta t$  denoting the time step. Let  $N_T = T/\Delta t$  be the number of uniform subdivisions in [0, T]. For any  $n = 0, 1, ..., N_T - 1$ , we utilize the superscript n to indicate variables that are evaluated at time  $t^n$  so that, for example,  $u^n := u(x, t^n)$  and  $y^n := y(t^n)$ .

#### 4.1. Functional iteration methods

The technique of functional iterations consists in decoupling the PDE and ODE problems and solving them sequentially until convergence in order to advance from a given time level to the next. Two choices of functional iteration methods are considered in this article, the difference between the two laying in the treatment of the interface unknowns P and Q. The two choices are denoted by PQP and QPQ subiterations and are detailed in Sections 4.1.1 and 4.1.2, respectively. These choices are conceptually similar to the Dirichlet-Neumann and Neumann-Dirichlet approaches that are utilized in domain decomposition methods (see [56]), as discussed below.

# 4.1.1. PQP subiterations

Let  $j \ge 0$  be an integer representing the functional iteration counter. In the PQP subiterations, at each discrete time level  $t^n$ , the Biot PDE model is solved first using  $P_{(j)}$  as a (given) input in (7c) to compute the new value  $Q_{(j+1)}$  of the interface variable Q. Then, the ODE model for the lumped hydraulic circuit  $\Upsilon$  is solved using  $Q_{(j+1)}$  as a given input in (5). Finally, relationship (8) allows the calculation of the new value  $P_{(j+1)}$  of the interface variable P. The iterative process continues until a convergence criterion on the distance between  $P_{(j)}$  and  $P_{(j+1)}$  is satisfied up to a given tolerance. The method is schematically illustrated in Fig. 2.

The time advancement from  $t^n$  to  $t^{n+1}$  using the PQP subiterations consists of executing sequentially the following three steps for j = 0, 1, ... until convergence:

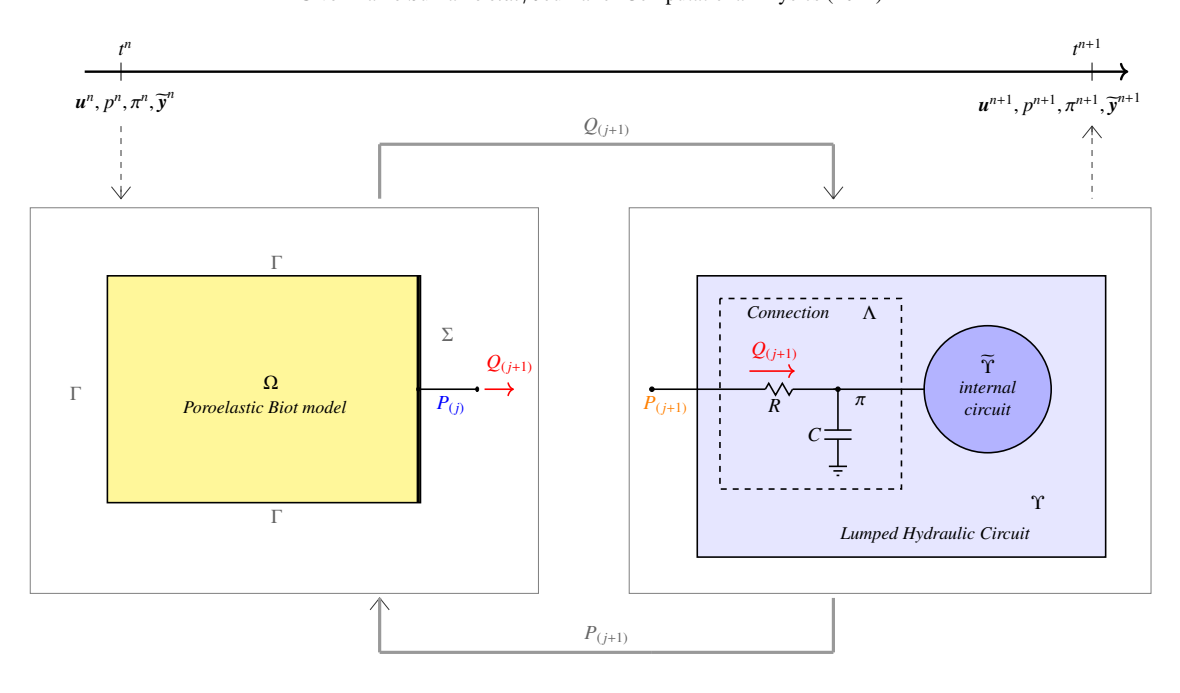


Fig. 2: This figure schematically illustrates the PQP subiterations for the solution of the coupled PDE-ODE model. At each time level  $t^n$ , an iterative process characterized by the iteration counter  $j \ge 0$  is conducted as follows. The interface variable  $P_{(j)}$  is used as an input for the PDE model to compute an updated value  $Q_{(j+1)}$  of the interface variable Q. Then,  $Q_{(j+1)}$  is used as an input for the ODE model of the lumped circuit  $\Upsilon$  to compute an updated value  $P_{(j+1)}$  of the interface variable P. The process is stopped when a convergence criterion on the distance between  $P_{(j)}$  and  $P_{(j+1)}$  is satisfied up to a given tolerance.

# **Step 1.** Given $u^n$ and $P_{(i)}$ solve:

$$\nabla \cdot \boldsymbol{u}_t - \nabla \cdot (k \nabla p) = S \qquad \text{in } \Omega \times (t^n, t^{n+1}), \tag{25a}$$

$$\nabla \cdot \mathbf{T}(\boldsymbol{u}, p) + \boldsymbol{f} = \mathbf{0} \qquad \text{in } \Omega \times (t^n, t^{n+1}), \tag{25b}$$

with the boundary conditions:

$$\mathbf{T} \, \boldsymbol{n} = \boldsymbol{g}, \qquad \qquad \boldsymbol{v} \cdot \boldsymbol{n} = 0, \qquad \qquad \operatorname{on} \, \Gamma_N \times (t^n, t^{n+1}), \tag{26a}$$

$$u = 0,$$
 on  $\Gamma_{D,p} \times (t^n, t^{n+1}),$  (26b)

$$\boldsymbol{u} = \boldsymbol{0}, \qquad \boldsymbol{v} \cdot \boldsymbol{n} = \psi, \qquad \text{on } \Gamma_{D,v} \times (t^n, t^{n+1}), \qquad (26c)$$

$$(\mathbf{T} \mathbf{n}) \cdot \boldsymbol{\tau}_1 = 0, \qquad (\mathbf{T} \mathbf{n}) \cdot \boldsymbol{\tau}_2 = 0, \qquad \text{on } \Gamma_0 \times (t^n, t^{n+1}), \qquad (26d)$$

$$\boldsymbol{u} \cdot \boldsymbol{n} = 0,$$
 on  $\Gamma_0 \times (t^n, t^{n+1}),$  (26e)

$$\mathbf{u} = \mathbf{0} \qquad \text{on } \Sigma \times (t^n, t^{n+1}), \tag{26f}$$

$$p(\mathbf{x}, t) = P_{(i)} \qquad \text{on } \Sigma \times (t^n, t^{n+1}). \tag{26g}$$

and the initial condition

$$\boldsymbol{u}(\boldsymbol{x},t^n) = \boldsymbol{u}^n \tag{27}$$

and then set

$$Q_{(j+1)} = -k \int_{\Sigma} \nabla p(\mathbf{x}, t^{n+1}) \cdot \mathbf{n}(\mathbf{x}) d\mathbf{x}$$
 (28)

# **Step 2.** Given $y^n$ and $Q_{(i+1)}$ solve

$$\frac{dy(t)}{dt} = \mathbf{A}y(t) + s(t) + \mathbf{b}(Q_{(j+1)}) \qquad \text{in } (t^n, t^{n+1}), \tag{29a}$$

with the initial condition

$$\mathbf{v}(t^n) = \mathbf{v}^n \tag{29b}$$

and then set

$$P_{(i+1)} = \pi(t^{n+1}) + R Q_{(i+1)}$$
(30)

where  $\pi(t^{n+1}) = \mathbf{v}(t^{n+1}) \cdot \mathbf{e}_1$ .

## Step 3. Check the condition

$$d(P_{(i)}, P_{(i+1)}) < tol_P \tag{31}$$

where  $tol_P$  is a given tolerance and  $d(P_{(j)}, P_{(j+1)})$  is the distance between  $P_{(j)}$  and  $P_{(j+1)}$ . If (31) is satisfied, then set

$$\mathbf{u}^{n+1} := \mathbf{u}(\mathbf{x}, t^{n+1}), \quad p^{n+1} := p(\mathbf{x}, t^{n+1}), \quad Q^{n+1} := Q_{(j+1)},$$

as computed in Step 1, and

$$y^{n+1} = y(t^{n+1}), P^{n+1} := P_{(j+1)},$$

as computed in Step 2. Otherwise, advance j and repeat.

An initial value for  $P_{(j)}$  must be selected in order to fully characterize the PQP subiterations. If n = 0 we set  $P_{(0)} = P^0$ , where  $P^0$  is an initial guess, otherwise we set  $P_{(0)} = P^n$ . Furthermore, a definition of distance for assessing convergence must be adopted. Possible choices are the absolute and relative distances which, for any scalar variables  $z_{(j)}$  and  $z_{(j+1)}$ , are defined as follows:

$$d_{abs}(z_{(j)}, z_{(j+1)}) := |z_{(j+1)} - z_{(j)}| \tag{32}$$

$$d_{rel}(z_{(j)}, z_{(j+1)}) := \frac{|z_{(j+1)} - z_{(j)}|}{|z_{(j+1)}|}, \qquad z_{(j+1)} \neq 0.$$
(33)

We remark that the PQP subiterations described above are similar to the Dirichlet-Neumann approach in domain decomposition. A Dirichlet condition for the pressure, see Eq. (26g), is utilized in Step 1, whose solution is then used to update a Neumann condition of integral type, see Eq. (28), which is utilized as an input for Step 2, see Eq. (29a).

# 4.1.2. QPQ subiterations

At each discrete time level  $t^n$  of the QPQ subiterations, the Biot PDE model is solved first using  $Q_{(j)}$  as a (given) input in (7b) to compute the new value  $P_{(j+1)}$  of the interface variable P. Then, the ODE model for the lumped hydraulic circuit  $\Upsilon$  is solved using  $P_{(j+1)}$  as a given input. Finally, relationship (8) allows the calculation of the new value  $Q_{(j+1)}$  of the interface variable Q. The iterative process continues until a convergence criterion on the distance between  $Q_{(j)}$  and  $Q_{(j+1)}$  is satisfied up to a given tolerance. The method is schematically illustrated in Fig. 3.

In order to properly describe the QPQ subiterations, it is useful to utilize (8) and rewrite the vector valued function b(Q(t)) introduced in (5) in the alternate form

$$b(Q(t)) = \beta(P(t)) + \mathbf{V} \mathbf{y}(t)$$
(34)

with

$$\boldsymbol{\beta}(P(t)) = \frac{P(t)}{RC} \boldsymbol{e}_1 \quad \text{and} \quad \mathbf{V} = \begin{bmatrix} -\frac{1}{RC} & 0 & \dots & 0 \\ 0 & 0 & \dots & 0 \\ \vdots & \vdots & \ddots & \vdots \\ 0 & 0 & \dots & 0 \end{bmatrix}$$
(35)

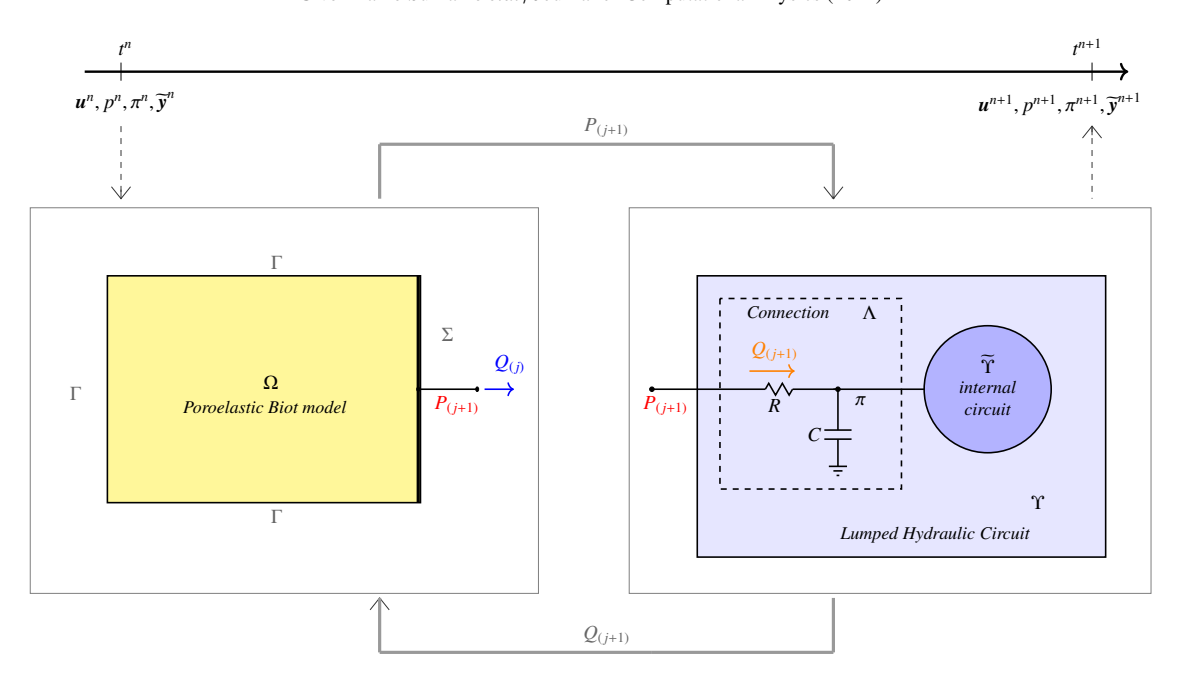


Fig. 3: This figure schematically illustrates the QPQ subiterations for the solution of the coupled PDE-ODE model. At each time level  $t^n$ , an iterative process characterized by the iteration counter  $j \ge 0$  is conducted as follows. The interface variable  $Q_{(j)}$  is used as an input for the PDE model to compute an updated value  $P_{(j+1)}$  of the interface variable P. Then,  $P_{(j+1)}$  is used as an input for the ODE model of the hydraulic lumped circuit  $\Upsilon$  to compute an updated value  $Q_{(j+1)}$  of the interface variable Q. The process is stopped when a convergence criterion on the distance between  $Q_{(j)}$  and  $Q_{(j+1)}$  is satisfied up to a given tolerance.

Then, ODEsystem (4) can be rewritten as

$$\frac{d\mathbf{y}(t)}{dt} = (\mathbf{A} + \mathbf{V})\mathbf{y}(t) + \mathbf{s}(t) + \boldsymbol{\beta}(P(t)) \qquad \text{in } (0, T).$$
 (36)

The time advancement from  $t^n$  to  $t^{n+1}$  using the QPQ subiterations consists of executing sequentially the following three steps for  $j = 0, 1, \ldots$  until convergence:

# **Step 1.** Given $u^n$ and $Q_{(j)}$ solve:

$$\nabla \cdot \boldsymbol{u}_t - \nabla \cdot (k \nabla p) = S \qquad \text{in } \Omega \times (t^n, t^{n+1}), \tag{37a}$$

$$\nabla \cdot \mathbf{T}(\boldsymbol{u}, p) + \boldsymbol{f} = \mathbf{0} \qquad \text{in } \Omega \times (t^n, t^{n+1}), \tag{37b}$$

with the boundary conditions:

$$\mathbf{T} \, \boldsymbol{n} = \boldsymbol{g}, \qquad \qquad \boldsymbol{v} \cdot \boldsymbol{n} = 0, \qquad \qquad \text{on } \Gamma_N \times (t^n, t^{n+1}), \tag{38a}$$

$$u = 0,$$
 on  $\Gamma_{D,p} \times (t^n, t^{n+1}),$  (38b)

$$\boldsymbol{u} = \boldsymbol{0}, \qquad \boldsymbol{v} \cdot \boldsymbol{n} = \psi, \qquad \text{on } \Gamma_{D,v} \times (t^n, t^{n+1}), \qquad (38c)$$

$$(\mathbf{T} \mathbf{n}) \cdot \boldsymbol{\tau}_1 = 0, \qquad (\mathbf{T} \mathbf{n}) \cdot \boldsymbol{\tau}_2 = 0, \qquad \text{on } \Gamma_0 \times (t^n, t^{n+1}), \qquad (38d)$$

$$\boldsymbol{u} \cdot \boldsymbol{n} = 0,$$
 on  $\Gamma_0 \times (t^n, t^{n+1}),$  (38e)

$$\mathbf{u} = \mathbf{0} \qquad \text{on } \Sigma \times (t^n, t^{n+1}), \tag{38f}$$

$$\int_{\Sigma} \mathbf{v} \cdot \mathbf{n} \, d\mathbf{x} = Q_{(j)} \qquad \text{on } \Sigma \times (t^n, t^{n+1}), \tag{38g}$$

with the constraint that p is constant in space over  $\Sigma$ , namely

$$p(\mathbf{x}, t) = C(t), \qquad \text{on } \Sigma \times (t^n, t^{n+1})$$
(39)

where the function C(t) is part of the unknowns of the problem, and the initial condition

$$\boldsymbol{u}(\boldsymbol{x},t^n) = \boldsymbol{u}^n \tag{40}$$

and then set

$$P_{(j+1)} = C(t^{n+1}). (41)$$

**Step 2.** Given  $y^n$  and  $P_{(i+1)}$  solve

$$\frac{d\mathbf{y}(t)}{dt} = (\mathbf{A} + \mathbf{V})\mathbf{y}(t) + \mathbf{s}(t) + \boldsymbol{\beta}(P_{(j+1)}) \qquad \text{in } (t^n, t^{n+1}), \tag{42a}$$

with the initial condition

$$\mathbf{y}(t^n) = \mathbf{y}^n \tag{42b}$$

and then set

$$Q_{(j+1)} = \frac{P_{(j+1)} - \pi(t^{n+1})}{R} \tag{43}$$

where  $\pi(t^{n+1}) = \mathbf{y}(t^n) \cdot \mathbf{e}_1$ .

#### **Step 3.** Check the condition

$$d(Q_{(i)}, Q_{(i+1)}) < tol_Q \tag{44}$$

where  $tol_Q$  is a given tolerance and  $d(Q_{(j)}, Q_{(j+1)})$  is the distance between  $Q_{(j)}$  and  $Q_{(j+1)}$ . Possible options are the absolute and relative distances defined in (32) and (33). If (44) is satisfied, then set

$$u^{n+1} := u(x, t^{n+1}), \quad p^{n+1} := p(x, t^{n+1}), \quad P^{n+1} := P_{(j+1)},$$

as computed in Step 1, and

$$\mathbf{y}^{n+1} = \mathbf{y}(t^{n+1}), \quad Q^{n+1} := Q_{(j+1)},$$

as computed in Step 2. Otherwise, advance j and repeat.

An initial value for  $Q_{(j)}$  must be selected in order to fully characterize the QPQ subiterations. If n = 0 we set  $Q_{(0)} = Q^0$ , where  $Q^0$  is an initial guess, otherwise we set  $Q_{(0)} = Q^n$ . We remark that the QPQ subiteration method described above is similar to the Neumann-Dirichlet approach in domain decomposition. A Neumann condition of integral type, see Eq. (38g), is utilized in Step 1, whose solution is then used to update the Dirichlet condition for the pressure at the interface, see Eq. (41), which is utilized as an input for Step 2, see Eq. (42a).

# 4.2. Operator splitting

The operator splitting method consists in splitting the original system into separate parts and establishing a communication among the parts through the initial conditions [57]. If the operator splitting is designed in such a way as to maintain at the discrete level the energy properties of the system, unconditional stability with respect to the choice of the time step may be achieved without the need of subiterations among the substeps [58, 59, 60, 61, 62, 63]. Inspired by the energy identity illustrated in Section 3, we propose to split the problem at hand by treating the interface coupling conditions together with the Biot model in a first substep, thereby ensuring mass conservation and pressure continuity at the interface, and solving the internal part of the circuit  $\tilde{\Upsilon}$  in the next substep, as illustrated in Fig. 4.

Then, for any  $n \ge 0$ , the proposed operator splitting method consists of solving sequentially the following two steps:

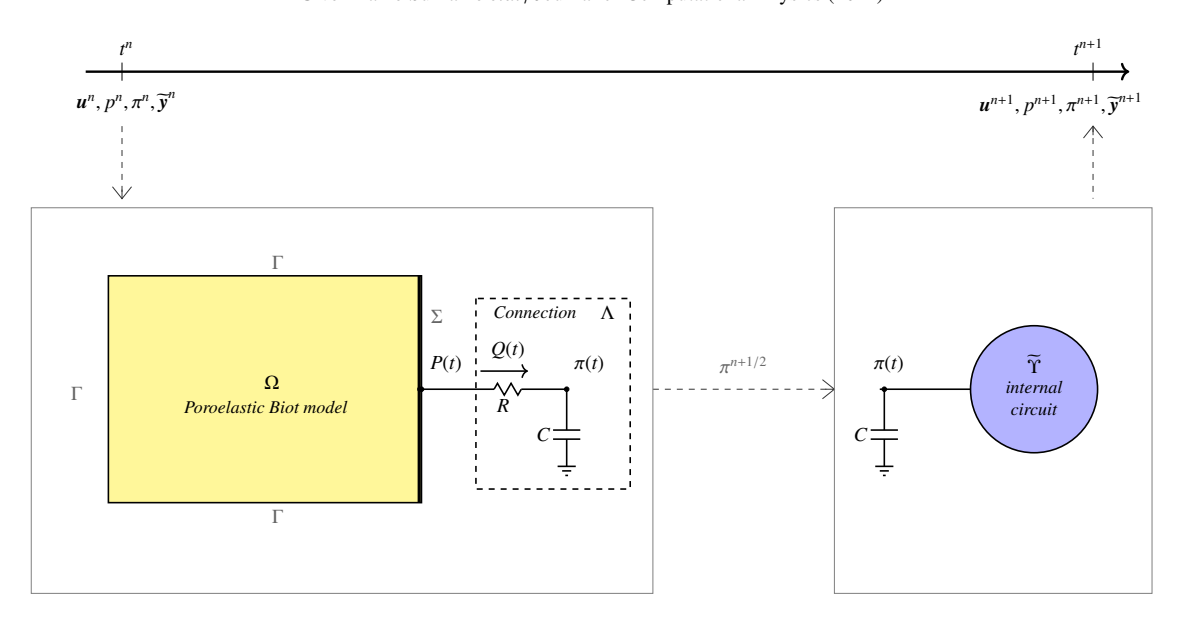


Fig. 4: This figure schematically illustrates the operator splitting method for the solution of the coupled PDE-ODE model. At each time level  $t^n$ , the Biot model in  $\Omega$  is solved together with the circuit connection  $\Lambda$  to compute an updated value  $\pi^{n+1/2}$  of the pressure at the connecting capacitor C, which is then used as initial condition for the ODE model that is solved next. The method does not require any subiteration between the steps.

# **Step 1.** Given $u^n$ and $y^n$ solve:

$$\nabla \cdot \boldsymbol{u}_t - \nabla \cdot (k \nabla p) = S \qquad \text{in } \Omega \times (t^n, t^{n+1}), \tag{45}$$

$$\nabla \cdot \mathbf{T}(\boldsymbol{u}, p) + \boldsymbol{f} = \mathbf{0} \qquad \text{in } \Omega \times (t^n, t^{n+1}), \tag{46}$$

$$\frac{d\mathbf{y}}{dt} = \mathbf{b}(Q(t)) \qquad \qquad \text{in } (t^n, t^{n+1}), \tag{47}$$

with the boundary conditions:

$$\mathbf{T} \, \boldsymbol{n} = \boldsymbol{g}, \qquad v \cdot \boldsymbol{n} = 0, \qquad \text{on } \Gamma_N \times (t^n, t^{n+1}), \tag{48a}$$

$$u = 0,$$
 on  $\Gamma_{D,p} \times (t^n, t^{n+1}),$  (48b)

$$\boldsymbol{u} = \boldsymbol{0}, \qquad \boldsymbol{v} \cdot \boldsymbol{n} = \psi, \qquad \text{on } \Gamma_{D,v} \times (t^n, t^{n+1}),$$
 (48c)

$$(\mathbf{T} \mathbf{n}) \cdot \boldsymbol{\tau}_1 = 0, \qquad (\mathbf{T} \mathbf{n}) \cdot \boldsymbol{\tau}_2 = 0, \qquad \text{on } \Gamma_0 \times (t^n, t^{n+1}), \qquad (48d)$$

$$\boldsymbol{u} \cdot \boldsymbol{n} = 0,$$
 on  $\Gamma_0 \times (t^n, t^{n+1}),$  (48e)

the interface conditions:

$$\mathbf{u} = \mathbf{0} \qquad \qquad \text{on } \Sigma \times (t^n, t^{n+1}), \tag{49}$$

$$\int_{\Sigma} \mathbf{v} \cdot \mathbf{n} = Q(t) \qquad \text{on } \Sigma \times (t^n, t^{n+1}), \tag{50}$$

$$p(\mathbf{x},t) = P(t) \qquad \text{on } \Sigma \times (t^n, t^{n+1}), \tag{51}$$

$$Q(t) = \frac{P(t) - \pi(t)}{R} \qquad \text{on } \Sigma \times (t^n, t^{n+1}), \tag{52}$$

and the initial conditions:

$$\mathbf{u} = \mathbf{u}^n$$
 in  $\Omega$  at  $t = t^n$  (53)

$$y = y^n at t = t^n. (54)$$

Then set  $u^{n+1/2} = u(t^{n+1})$ ,  $p^{n+1/2} = p(t^{n+1})$  and  $y^{n+1/2} = y(t^{n+1})$ .

**Step 2.** Given  $\mathbf{v}^{n+1/2}$ , solve

$$\frac{d\mathbf{y}}{dt} = \mathbf{A}\mathbf{y} + \mathbf{s}(t) \qquad \qquad \text{in } (t^n, t^{n+1}), \tag{55}$$

with the initial condition

$$y = y^{n+1/2}$$
 at  $t = t^n$  (56)

Then set  $y^{n+1} = y(t^{n+1})$ . Since u and p are not updated in this step, we also have  $u^{n+1} = u^{n+1/2}$  and  $p^{n+1} = p^{n+1/2}$ .

It is interesting to notice that the definitions of y(t) and b(Q(t)) given in (3) and (5), respectively, reduce Eq. (47) to the single scalar equation

$$\frac{d\pi(t)}{dt} = \frac{Q(t)}{C} \tag{57}$$

thereby effectively making the value of  $\pi$  at the end of Step 1, namely  $\pi^{n+1/2}$ , the pivotal link in the communication between the two steps, as illustrated in Fig. 4. We emphasize that the splitting algorithm illustrated above does not include any convergence criterium, since the two steps are solved sequentially without subiterations. We also note that we have opted for solving the PDE problem in the Step 1 and the ODE problem in Step 2. However, this choice is not binding and the order of the steps may be switched.

# 5. 1D-0D example of coupled Biot-circuit system

In this section, we present a 1D-0D version of the 3D-0D coupled Biot-circuit model that can be used to easily study and compare the performance of the methods based on functional iterations and operator splitting illustrated in Section 4. Let us consider the Biot domain  $\Omega$  to be given by  $\Omega = (x, y, z) \in (0, c) \times (-a/2, a/2) \times (-b/2, b/2)$ , as illustrated in Fig. 5. The boundary of  $\Omega$  is  $\partial \Omega = \Gamma_N \cup \Gamma_0 \cup \Sigma$ , with  $\Gamma_0 = \Gamma_0^t \cup \Gamma_0^b \cup \Gamma_0^t \cup \Gamma_0^r$  representing the lateral surface. The symbol W in Fig. 5 represents the point on the surface  $\Sigma$  at which the lumped hydraulic circuit of Fig. 6 is physically connected to the domain  $\Omega$ .

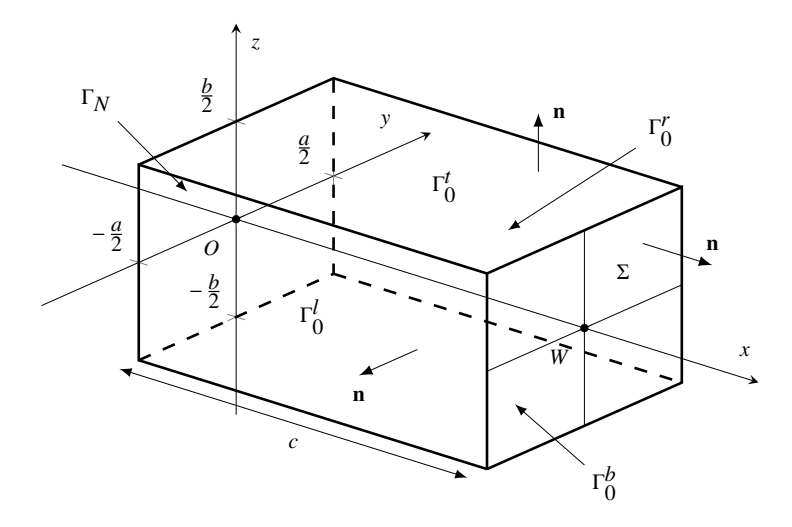


Fig. 5: The three-dimensional domain  $\Omega$  and the geometrical notation. The domain boundary is  $\partial \Omega = \Gamma_N \cup \Gamma_0 \cup \Sigma$ , with  $\Gamma_0 = \Gamma_0^l \cup \Gamma_0^$ 

Let us assume that the solid displacement u consists of the sole component u along the x-direction, and that u and

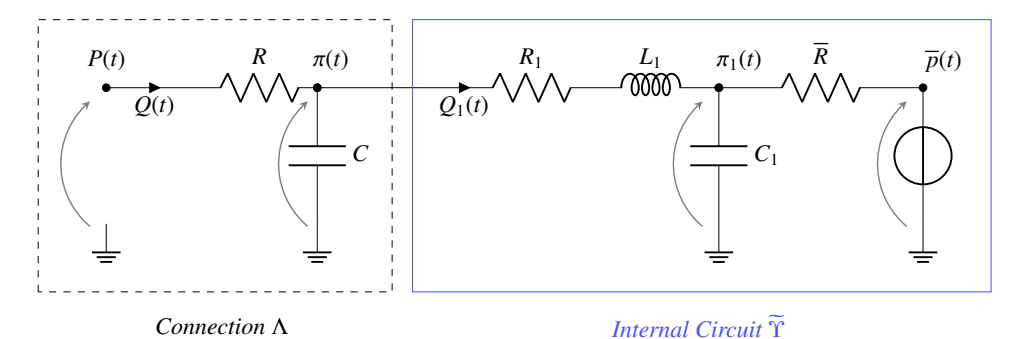


Fig. 6: Schematic representation of the lumped hydraulic circuit  $\Upsilon$ . The connection  $\Lambda$  is composed of the linear time-invariant resistor R and the linear time-invariant capacitor C. The internal circuit  $\widetilde{\Upsilon}$  is composed of one linear time-invariant capacitor  $C_1$ , one linear time-invariant inductor,  $L_1$ , two linear time-invariant resistors,  $R_1$  and  $\overline{R}$ , and one pressure source,  $\overline{p} = \overline{p}(t)$ .

p are functions of x and t. Consequently, we can write:

$$\mathbf{v} = -k\nabla p = \left[ -k\frac{\partial p(x,t)}{\partial x}, \, 0, \, 0 \right]^T \tag{58a}$$

$$\mathbf{T}(\boldsymbol{u}, p) = \begin{bmatrix} K \frac{\partial u(x,t)}{\partial x} - p(x,t) & 0 & 0\\ 0 & \lambda \frac{\partial u(x,t)}{\partial x} - p(x,t) & 0\\ 0 & 0 & \lambda \frac{\partial u(x,t)}{\partial x} - p(x,t) \end{bmatrix}$$
(58b)

where  $K := \lambda + 2\mu$  is the aggregate modulus. It is easy to check that the boundary conditions (6d)-(6e) on  $\Gamma_0$  are automatically satisfied. The interface conditions to be enforced on the surface  $\Sigma$  are the same as in (7) and the initial conditions are the same as in (9).

It is worth noticing that relations (6d)-(6e) have a significant physical interpretation. The boundary conditions (6e) express the fact that the lateral surface is impermeable and may displace only in the tangential direction. The boundary conditions (6d) express the fact that the tangential stresses are equal to zero on the lateral surface  $\Gamma_0$ , thus preventing the occurrence of any shear body motion. The only nonvanishing stress on the lateral surface of the parallelepiped  $\Omega$  is the normal component of the traction  $\mathbf{T}n$ , equal to the sum of  $\lambda \partial u/\partial x$  and the compression -p due to the hydrostatic pressure; this normal stress keeps the body motion confined along the x-axis.

Having introduced the three-dimensional setting that supports a one-dimensional motion in the body  $\Omega$ , we are in the position to formulate the poroelastic Biot equations (1) as follows:

$$\frac{\partial}{\partial t} \left( \frac{\partial u(x,t)}{\partial x} \right) + \frac{\partial v(x,t)}{\partial x} = S, \qquad \text{for } x \in (0,c), \ t \in (0,T)$$
 (59a)

$$\frac{\partial \mathcal{T}(x,t)}{\partial x} + f = 0, \qquad \text{for } x \in (0,c), \ t \in (0,T)$$

$$v(x,t) = -k\frac{\partial p(x,t)}{\partial x}, \qquad \text{for } x \in (0,c), \ t \in (0,T)$$
 (59c)

$$\mathcal{T}(x,t) = K \frac{\partial u(x,t)}{\partial x} - p(x,t), \qquad \text{for } x \in (0,c), \ t \in (0,T)$$
 (59d)

subject to the initial condition

$$u(x, 0) = y(x),$$
 for  $x \in (0, c)$  (59e)

where  $\chi = \chi(x)$  is a given function. The equation system (59) is complemented by the boundary conditions:

$$K\frac{\partial u(0,t)}{\partial x} - p(0,t) = -g(t), \qquad t \in (0,T), \tag{60a}$$

$$\frac{\partial p(0,t)}{\partial x} = 0, t \in (0,T), (60b)$$

and the interface conditions:

$$u(c,t) = 0,$$
  $t \in (0,T),$  (61a)

$$v(c,t) = \frac{Q(t)}{ab}, \qquad t \in (0,T), \tag{61b}$$

$$p(c,t) = P(t)$$
.  $t \in (0,T)$ . (61c)

Let us now focus on the lumped hydraulic circuit coupled with the one-dimensional Biot model. In this specific example, we consider the circuit  $\Upsilon$  illustrated in Fig. 6, for which the vector  $\mathbf{y}(t) \in \mathbb{R}^3$  of state variables is defined as

$$y(t) = [\pi(t), \pi_1(t), Q_1(t)]^T,$$
 (62a)

so that the vector of state variables  $\widetilde{y}(t) \in \mathbb{R}^2$  for the internal circuit  $\widetilde{\Upsilon}$  is

$$\widetilde{\mathbf{y}}(t) = [\pi_1(t), Q_1(t)]^T \tag{62b}$$

and the matrix A is given by

$$\mathbf{A} = \begin{bmatrix} 0 & 0 & -\frac{1}{C} \\ 0 & -\frac{1}{\overline{R}C_1} & \frac{1}{C_1} \\ \frac{1}{L_1} & -\frac{1}{L_1} & -\frac{R_1}{L_1} \end{bmatrix}. \tag{62c}$$

It can be checked that matrix **A** is nonsingular. The vectors s(t) and b(Q(t)) are defined as

$$s(t) = \left[0, \frac{\overline{p}(t)}{\overline{R}C_1}, 0\right]^T \quad \text{and} \quad \boldsymbol{b}(Q(t)) = \left[\frac{Q(t)}{C}, 0, 0\right]^T$$
 (62d)

with

$$Q(t) = \frac{P(t) - \pi(t)}{R}.$$
(62e)

Following (15), the matrix U for this circuit is defined as follows

$$\mathbf{U} = \begin{bmatrix} C & 0 & 0 \\ 0 & C_1 & 0 \\ 0 & 0 & L_1 \end{bmatrix}. \tag{62f}$$

The circuit dynamics is described by the first order, nonhomogeneous linear system of differential equations of the form (4), whose solution can be written as

$$\mathbf{y}(t) = e^{t\mathbf{A}}\mathbf{y}_0 + \int_0^t e^{(t-s)\mathbf{A}} \left[ \mathbf{s}(s) + \mathbf{b}(Q(s)) \right] ds$$
 (63)

where  $y_0$  is the initial condition.

## 6. Main theorems: numerical properties of functional iterations and operator splitting methods

The functional iteration methods based on PQP and QPQ subiterations rely on seeking the fixed point of suitable mappings within a discrete time interval  $(t^n, t^{n+1})$ , as detailed in Section 4. However, it is well known that, depending on the mathematical properties of such mappings, it may or may not be possible to achieve convergence to the fixed

point (see [55, 64, 65]). In this section, Theorems 1 and 2 provide sufficient conditions for the convergence of PQP and QPQ subiterations applied to the 1D-0D coupled problem described in Section 5 discretized in time via a Backward Euler method.

The operator splitting method does not require subiterations within each time step. Thus, instead of studying its convergence, we focus on the stability of the numerical solution as a function of the time discretization step  $\Delta t$ . In this section, Theorem 3 shows that the proposed operator splitting scheme in its general formulation illustrated in Section 4.2 in the absence of external forcing is unconditionally stable with respect to  $\Delta t$ .

**Theorem 1** (Convergence of PQP subiterations). Let us consider the 1D-0D coupled problem described in Section 5 discretized in time via a Backward Euler method. In this case, a sufficient condition for the convergence of the PQP subiterations is

$$|\gamma_2(\Delta t)| = \left| \frac{1}{\beta_1(\Delta t)} \left( \frac{\Delta t N_{11}(\Delta t)}{C} + R \right) \right| < 1 \tag{64}$$

where

$$\beta_1(\Delta t) = \frac{\coth(c\xi)}{kab\xi}$$
 with  $\xi = \sqrt{\frac{1}{kK\Delta t}}$ 

and

$$N_{11}(\Delta t) = (\mathbf{N}e_1)e_1$$
 with  $\mathbf{N}(\Delta t) = [\mathbf{I} - \Delta t\mathbf{A}]^{-1}$ .

*Proof.* To prove this theorem, we are going to obtain an explicit expression for the mapping  $P = \phi(P)$  characterizing the PQP subiterations in the case of the 1D-0D coupled problem described in Section 5 discretized in time via a Backward Euler method. The time-discrete version of the 1D Biot problem (115) reads

$$\frac{p^{n+1}(x) - p^n(x)}{\Delta t} - kKp_{xx}^{n+1}(x) = g'(t^{n+1}) \qquad x \in (0, c), \ n = 0, \dots, N_T - 1$$
 (65a)

$$p_x^{n+1}(0) = 0 (65b)$$

$$p_x^{n+1}(c) = -\frac{Q^{n+1}}{kab}. (65c)$$

We recall that  $\Delta t$  is the discrete time step,  $t^n = n\Delta t$  for  $n = 0, \dots, N_T - 1$ , with the superscripts n and n + 1 indicating that the specific variable is evaluated at  $t^n$  or  $t^{n+1}$ , respectively, and  $p^n(x)$  is given. Problem (65) can be solved in closed form to obtain

$$p^{n+1}(x) = (-\alpha_1 Q^{n+1} + \alpha_2)(e^{\xi x} + e^{-\xi x}) + \frac{e^{\xi x}}{2\xi} \int_0^x e^{-\xi s} f(s) ds - \frac{e^{-\xi x}}{2\xi} \int_0^x e^{\xi s} f(s) ds$$
 (66)

where

$$\begin{split} \xi &= \sqrt{\frac{1}{kK\Delta t}} \\ \alpha_1 &= \frac{1}{kab\xi(e^{\xi c} - e^{-\xi c})} \\ \alpha_2 &= -\frac{1}{\xi(e^{\xi c} - e^{-\xi c})} \left(\frac{e^{\xi c}}{2} \int_0^c e^{-\xi s} f(s) ds - \frac{e^{-\xi c}}{2} \int_0^c e^{\xi s} f(s) ds\right) \\ f(s) &= -\frac{1}{kK} \left(\frac{p^n}{\Delta t} + g'(t^{n+1})\right). \end{split}$$

Leveraging the fact that the pressure  $P^{n+1}$  at the 1D-0D interface at time  $t^{n+1}$  can be obtained as  $P^{n+1} = p^{n+1}(c)$ , we can evaluate (66) at x = c to obtain

$$P^{n+1} = -\beta_1(\Delta t) Q^{n+1} + \beta_2(\Delta t)$$
 (67)

where

$$\beta_1(\Delta t) = \frac{\coth(c\xi)}{kab\xi} \tag{68}$$

$$\beta_2(\Delta t) = \alpha_2(e^{\xi c} + e^{-\xi c}) + \frac{e^{\xi c}}{2\xi} \int_0^c e^{-\xi s} f(s) ds - \frac{e^{-\xi c}}{2\xi} \int_0^c e^{\xi s} f(s) ds.$$
 (69)

As a note, it is not surprising that, given the linear nature of the problem, the relationship (67) between  $P^{n+1}$  and  $Q^{n+1}$  is linear. However, it is important to notice that the parameters in this linear relationship depend nonlinearly on the time discretization parameter  $\Delta t$ .

Let us now consider the Backward Euler discretization of the lumped circuit. Starting from the formulation in (4), the discrete problem reads

$$\frac{\mathbf{y}^{n+1} - \mathbf{y}^n}{\Delta t} = \mathbf{A} \, \mathbf{y}^{n+1} + \mathbf{s}^{n+1} + \mathbf{b}(Q^{n+1}) \qquad \qquad n = 0, \dots, N_T - 1$$
 (70)

with  $y^n$  given. Solving equation (70) for  $y^{n+1}$  we obtain

$$\mathbf{y}^{n+1} = \mathbf{N}(\Delta t) \left( \boldsymbol{\omega}(\Delta t) + \Delta t \, \boldsymbol{b}(Q^{n+1}) \right) \tag{71}$$

with  $\mathbf{N}(\Delta t) = [\mathbf{I} - \Delta t \mathbf{A}]^{-1}$  and  $\omega(\Delta t) = y^n + \Delta t s^{n+1}$ , both functions of  $\Delta t$ . Observing that  $\pi^{n+1} = y^{n+1} \cdot e_1$  and  $b(Q^{n+1}) \cdot e_1 = Q^{n+1}/C$ , we can write

$$\pi^{n+1} = (\mathbf{N}(\Delta t)\,\omega)(\Delta t) \cdot \mathbf{e}_1 + \frac{\Delta t N_{11}(\Delta t)}{C} Q^{n+1} \tag{72}$$

where  $N_{11}(\Delta t) = (Ne_1)e_1$ .

The PQP subiterations compute the approximate solution of the coupled problem at time  $t^{n+1}$  by:

1. solving the Biot problem for a given interface pressure  $P_{(j)}^{n+1}$  to update the value of the interface flow rate  $Q_{(j+1)}^{n+1}$ ; in particular, Eq. (67) allows us to write

$$Q_{(j+1)}^{n+1} = -\frac{1}{\beta_1(\Delta t)} P_{(j)}^{n+1} + \frac{\beta_2(\Delta t)}{\beta_1(\Delta t)};$$
(73a)

2. utilizing the updated value  $Q_{(j+1)}^{n+1}$  to compute the solution of the lumped circuit; in particular, Eq. (72) allows us to write

$$\pi_{(j+1)}^{n+1} = (\mathbf{N}(\Delta t)\,\boldsymbol{\omega}(\Delta t)) \cdot \boldsymbol{e}_1 + \frac{\Delta t N_{11}(\Delta t)}{C} Q_{(j+1)}^{n+1}; \tag{73b}$$

3. updating the value of  $P_{(j+1)}^{n+1}$  via Poiseuille's law so that we can write

$$P_{(j+1)}^{n+1} = \pi_{(j+1)}^{n+1} + RQ_{(j+1)}^{n+1}$$
(73c)

until convergence. Combining the steps in (73) leads us to write the PQP subiterations in the form of a fixed-point algorithm as

$$P_{(j+1)}^{n+1} = \phi(P_{(j)}^{n+1}) \quad j \ge 0, \tag{74}$$

where the mapping  $\phi$  is defined as

$$\phi(s) = \gamma_1(\Delta t) - \gamma_2(\Delta t)s \tag{75}$$

with:

$$\gamma_1(\Delta t) = (\mathbf{N}(\Delta t)\,\boldsymbol{\omega}) \cdot \boldsymbol{e}_1 + \beta_2(\Delta t)\gamma_2(\Delta t)$$
$$\gamma_2(\Delta t) = \frac{1}{\beta_1(\Delta t)} \left(\frac{\Delta t N_{11}(\Delta t)}{C} + R\right).$$

A sufficient condition for the sequence  $\{P_{(j)}^{n+1}\}$  generated by (74) to converge is that  $|\phi'(s)| = |\gamma_2| < 1$ , where the apostrophe denotes the ordinary derivative with respect to the independent variable. Thus, a sufficient condition for convergence of the PQP subiterations is given by

$$|\gamma_2(\Delta t)| = \left| \frac{1}{\beta_1(\Delta t)} \left( \frac{\Delta t N_{11}(\Delta t)}{C} + R \right) \right| < 1.$$

 $10^{-1}$   $10^{-2}$   $10^{-2}$   $10^{-6}$   $10^{-5}$   $10^{-4}$   $10^{-3}$   $0^{-2}$   $10^{-2}$   $10^{-1}$   $10^{-1}$   $10^{-2}$   $10^{-1}$   $10^{-1}$   $10^{-1}$ 

Fig. 7: Plot of  $|\gamma_2(\Delta t)|$  for the choice of parameters shown in Table 2.

Fig. 7 shows the plot of  $|\gamma_2|$  as a function of the time discretization parameter  $\Delta t$  in the case where the values of model parameters are as reported in Table 2. We notice that the dependence of  $\gamma_2$  on  $\Delta t$  is nontrivial and it gives rise to a non-monotonic behavior that leads to unexpected consequences on the convergence of the PQP subiterations. In particular, we can see that, for this particular set of model parameters, the sufficient condition is not satisfied if  $\Delta t$  becomes too small, thereby hindering the hope of achieving convergence by following the usual strategy of decreasing the time step. Even though the fact that a sufficient condition is not satisfied does not necessarily mean that convergence is not achieved, the numerical experiments conducted in Section 8 actually show that the PQP subiterations fail to converge when  $\Delta t = 0.02$  s and converge when  $\Delta t = 0.1$  s. Moreover, in the case of failed convergence, simulations show that the discrete counterpart of the important coupling term in the energy identity given in Eq. (24) does not have the sign of a dissipation, as expected from the physics of the problem at the continuous level. Considerations related to the energy identity role in the case of PQP iterations are also discussed in Section 7.

**Theorem 2** (Convergence of QPQ subiterations). Consider the 1D-0D coupled problem described in Section 5 discretized in time via a Backward Euler method. In this case, a sufficient condition for the convergence of the QPQ subiterations is

$$|\alpha_2(\Delta t)| = \left| \frac{\beta_1(\Delta t)}{R} \left( 1 - \frac{\Delta t M_{11}(\Delta t)}{RC} \right) \right| < 1 \tag{76}$$

where

$$\beta_1(\Delta t) = \frac{\coth(c\xi)}{kab\xi} \quad with \quad \xi = \sqrt{\frac{1}{kK\Delta t}}$$

and

$$M_{11}(\Delta t) = (\mathbf{M} \mathbf{e}_1) \mathbf{e}_1$$
 with  $\mathbf{M}(\Delta t) = [\mathbf{I} - \Delta t(\mathbf{A} + \mathbf{V})]^{-1}$ .

*Proof.* To prove this theorem, we are going to obtain an explicit expression for the mapping  $Q = \psi(Q)$  characterizing the QPQ subiterations in the case of the 1D-0D coupled problem described in Section 5 discretized in time via a

Backward Euler method. We consider here the same time-discrete version of the 1D Biot problem that was utilized in Theorem 1 and, consequently, we can leverage relationship (67) between  $P^{n+1}$  and  $Q^{n+1}$ . However, the lumped circuit must be considered in its alternate formulation (36), whose time discretization via the Backward Euler method reads

$$\frac{\mathbf{y}^{n+1} - \mathbf{y}^n}{\Delta t} = (\mathbf{A} + \mathbf{V}) \, \mathbf{y}^{n+1} + \mathbf{s}^{n+1} + \boldsymbol{\beta}(P^{n+1}) \qquad \qquad n = 0, \dots, N_T - 1$$
 (77)

with  $y^n$  given. Solving equation (77) for  $y^{n+1}$  we obtain

$$\mathbf{y}^{n+1} = \mathbf{M}(\Delta t) \left( \omega(\Delta t) + \Delta t \, \boldsymbol{\beta}(P^{n+1}) \right) \tag{78}$$

with  $\mathbf{M}(\Delta t) = [\mathbf{I} - \Delta t(\mathbf{A} + \mathbf{V})]^{-1}$  and  $\omega(\Delta t) = y^n + \Delta t \, s^{n+1}$ , both depending on  $\Delta t$ . Observing that  $\pi^{n+1} = y^{n+1} \cdot \boldsymbol{e}_1$  and  $\mathbf{M}(\Delta t)\boldsymbol{\beta}(P^{n+1}) \cdot \boldsymbol{e}_1 = M_{11}(\Delta t)P^{n+1}/(RC)$ , where  $M_{11}(\Delta t) = (\mathbf{M}\boldsymbol{e}_1)\boldsymbol{e}_1$ , we can perform the scalar product of (78) by  $\boldsymbol{e}_1$  to obtain

$$\pi^{n+1} = (\mathbf{M}(\Delta t)\,\boldsymbol{\omega}(\Delta t)) \cdot \boldsymbol{e}_1 + \frac{\Delta t M_{11}(\Delta t)}{RC} P^{n+1} \,. \tag{79}$$

The QPQ iterations compute the approximate solution of the coupled problem at time  $t^{n+1}$  by:

1. solving the Biot problem for a given interface flow rate  $Q_{(j)}^{n+1}$  to update the value of the interface pressure  $P_{(j+1)}^{n+1}$ ; in particular, Eq. (67) allows us to write

$$P_{(j+1)}^{n+1} = -\beta_1(\Delta t) Q_{(j)}^{n+1} + \beta_2(\Delta t);$$
(80a)

2. utilizing the updated value  $P_{(j+1)}^{n+1}$  to compute the solution of the lumped circuit; in particular, Eq. (79) allows us to write

$$\pi_{(j+1)}^{n+1} = (\mathbf{M}(\Delta t)\,\boldsymbol{\omega}(\Delta t)) \cdot \boldsymbol{e}_1 + \frac{\Delta t M_{11}(\Delta t)}{RC} P_{(j+1)}^{n+1}; \tag{80b}$$

3. updating the value of  $Q_{(i+1)}^{n+1}$  via Poiseuille's law so that we can write

$$Q_{(j+1)}^{n+1} = \frac{P_{(j+1)}^{n+1} - \pi_{(j+1)}^{n+1}}{R}$$
(80c)

until convergence. Combining the steps in (80) leads to write the QPQ subiterations under the form of a fixed-point algorithm as

$$Q_{(j+1)}^{n+1} = \psi(Q_{(j)}^{n+1}) \quad j \ge 0, \tag{81}$$

where the mapping  $\psi$  is defined as

$$\psi(s) = \alpha_1(\Delta t) - \alpha_2(\Delta t)s \tag{82}$$

with

$$\begin{split} \alpha_1(\Delta t) &= -\frac{1}{R}(\mathbf{M}(\Delta t)\,\boldsymbol{\omega}) \cdot \boldsymbol{e}_1 + \frac{\beta_2(\Delta t)}{\beta_1(\Delta t)}\alpha_2(\Delta t) \\ \alpha_2(\Delta t) &= \frac{\beta_1(\Delta t)}{R}\left(1 - \frac{\Delta t M_{11}(\Delta t)}{RC}\right). \end{split}$$

A sufficient condition for the sequence  $\{Q_{(j)}^{n+1}\}$  generated by (81) to converge is that  $|\psi'(s)| = |\alpha_2| < 1$ , leading to the following sufficient condition for convergence of the QPQ subiterations

$$|\alpha_2(\Delta t)| = \left| \frac{\beta_1(\Delta t)}{R} \left( 1 - \frac{\Delta t M_{11}(\Delta t)}{RC} \right) \right| < 1.$$

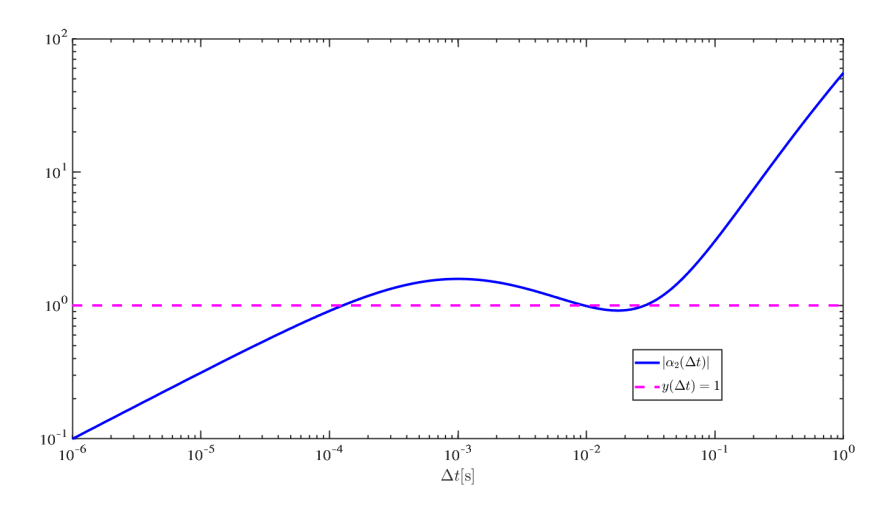


Fig. 8: Plot of  $|\alpha_2(\Delta t)|$  for the choice of parameters shown in Table 2.

Fig. 8 shows the plot of  $|\alpha_2|$  as a function of the time discretization parameter  $\Delta t$  in the case where the values of model parameters are as reported in Table 2. Also in this case, the dependence of  $\alpha_2$  on  $\Delta t$  is nontrivial and it gives rise to a non-monotonic behavior. In contrast with the case of PQP iterations, for this set of model parameters, the QPQ iterations are predicted to converge if  $\Delta t$  is less than  $10^{-4}$  s and if  $\Delta t$  is slightly larger than  $10^{-2}$  s. Numerical experiments conducted in Section 8 actually demonstrate that QPQ iterations converge for  $\Delta t = 0.02$  s and fail to converge for  $\Delta t = 0.1$  s, a value for which, instead, PQP iterations are predicted to converge. Also in this case, failure to converge is associated with a non-physical sign of the numerical counterpart of the dissipation term (24). Considerations related to the energy identity role in the case of QPQ iterations are also discussed in Section 7.

**Theorem 3** (Stability of operator splitting method). The operator splitting method illustrated in Section 4.2 for the solution of the multiscale interface coupled problem described in Section 2 in the absence of external forcing is unconditionally stable with respect to the choice of the time discretization step  $\Delta t$ .

*Proof.* To prove this theorem, we write the energy estimates associated with the problems introduced in the two steps separately and show that the operator splitting method does not disrupt the energy balance (23) that holds at the continuous level. This provides an a priori bound on the solution that ensures the desired unconditional stability. Henceforth, we will use superscripts I and I to distinguish between the unknown variables involved in the two steps of the splitting method.

We begin by considering the Biot system in Step 1 of the operator splitting method. Similarly to Section 3, we obtain the following energy identity

$$\frac{d}{dt}\mathcal{E}_{\Omega}(\boldsymbol{u}^{I}) + \mathcal{D}_{\Omega}(\boldsymbol{p}^{I}) = \mathcal{F}_{\Omega}(\boldsymbol{g}, \boldsymbol{\psi}; \boldsymbol{u}^{I}, \boldsymbol{p}^{I}) - P^{I}(t)Q^{I}(t)$$
(83)

where

$$\mathcal{E}_{\Omega}(\boldsymbol{u}^{I}) = \frac{\lambda}{2} \|\nabla \cdot \boldsymbol{u}^{I}\|_{L^{2}(\Omega)}^{2} + \mu \|\varepsilon(\boldsymbol{u}^{I})\|_{L^{2}(\Omega)}^{2}$$

$$\mathcal{D}_{\Omega}(p^I) = \|k^{1/2} \nabla p^I\|_{L^2(\Omega)}^2$$

$$\mathcal{F}_{\Omega}(\boldsymbol{g},\psi;\boldsymbol{u}^{I},p^{I}) = \int_{\Gamma_{N}} \boldsymbol{g} \cdot \boldsymbol{u}_{t}^{I} \, d\Gamma_{N} - \int_{\Gamma_{D,v}} \psi \, p^{I} \, d\Gamma_{D,v}.$$

We note that Step 1 also includes the following ODE

$$\frac{d\mathbf{y}^{I}}{dt} = \mathbf{b}(Q^{I}(t)) = \left[\frac{Q^{I}(t)}{C}, \mathbf{0}\right]^{T}$$

which simplifies to the following scalar ODE for  $\pi^I$ 

$$\frac{d\pi^I}{dt} = \frac{Q^I(t)}{C}$$

leading to the energy estimate

$$\frac{C}{2}\frac{d}{dt}(\pi^I)^2 = \pi^I Q^I. \tag{84}$$

Now we combine (83) with (84) and obtain the energy identity for the coupled system of Step 1

$$\frac{d}{dt} \left[ \mathcal{E}_{\Omega}(\boldsymbol{u}^{I}) + \frac{C}{2} (\boldsymbol{\pi}^{I})^{2} \right] + \mathcal{D}_{\Omega}(\boldsymbol{p}^{I}) + \mathcal{D}_{\Lambda}(\boldsymbol{Q}^{I}) = \mathcal{F}_{\Omega}(\boldsymbol{g}, \boldsymbol{\psi}; \boldsymbol{u}^{I}, \boldsymbol{p}^{I})$$
(85)

with

$$\mathcal{D}_{\Lambda}(Q^{I}) = R(Q^{I}(t))^{2}. \tag{86}$$

It is worth emphasizing that the choice to include the connecting part  $\Lambda$  of the lumped circuit within Step 1 along with the Biot problem ensures that the numerical counterpart of  $\mathcal{D}_{\Lambda}$  is nonnegative, thereby preserving the dissipative nature that this term has at the continuous level. Furthermore, in the absence of external forcing terms, i.e.  $\mathcal{F}_{\Omega}(\mathbf{g}, \psi; \mathbf{u}^{I}, p^{I}) = 0$ , it follows that for  $n \geq 0$ 

$$\left[\mathcal{E}_{\Omega}(\boldsymbol{u}^{I}(t^{n+1})) + \frac{C}{2}(\pi^{I}(t^{n+1}))^{2}\right] \leq \left[\mathcal{E}_{\Omega}(\boldsymbol{u}^{I}(t^{n})) + \frac{C}{2}(\pi^{I}(t^{n}))^{2}\right]. \tag{87}$$

We also notice that, since we are not updating the variables  $\Pi_i$  and  $Q_i$  in this step, we have  $\Pi_i^I(t^{n+1}) = \Pi_i^I(t^n)$  and  $Q_i^I(t^{n+1}) = Q_i^I(t^n)$  or, equivalently,  $\widetilde{\mathbf{y}}^I(t^{n+1}) = \widetilde{\mathbf{y}}^I(t^n)$ . Therefore we have for  $n \ge 0$ 

$$\left[\mathcal{E}_{\Omega}(\boldsymbol{u}^{l}(t^{n+1})) + \mathcal{E}_{\Upsilon}(\boldsymbol{y}^{l}(t^{n+1}))\right] \leq \left[\mathcal{E}_{\Omega}(\boldsymbol{u}^{l}(t^{n})) + \mathcal{E}_{\Upsilon}(\boldsymbol{y}^{l}(t^{n}))\right]. \tag{88}$$

Let us now consider Step 2 of the operator splitting method, where we need to solve the following ODE system

$$\frac{d\mathbf{y}^{II}}{dt} = \mathbf{A}\mathbf{y}^{II} + \mathbf{s}(t). \tag{89}$$

Using multiplier  $\mathbf{U}\mathbf{y}^{II}$  in the circuit ODE (89) we obtain the following identity

$$\frac{d\mathcal{E}_{\Upsilon}(\mathbf{y}^{II})}{dt} + \mathcal{D}_{\Upsilon}(\mathbf{y}^{II}) = \mathcal{F}^{II}(\mathbf{s}; \mathbf{y}^{II}), \tag{90}$$

where

$$\mathcal{E}_{\Upsilon}(\mathbf{y}^{II}) = \frac{C(\pi^{II})^2}{2} + \sum_{i=1}^{n_C} \frac{C_i(\Pi_i^{II})^2}{2} + \sum_{i=1}^{n_L} \frac{L_i(Q_i^{II})^2}{2}$$
(91)

is the energy stored in the capacitors and inductors within the circuit \( \cdot \). The dissipation in the circuit is given by

$$\mathcal{D}_{\Upsilon}(\mathbf{y}^{II}) = (\mathbf{B}\mathbf{y}^{II}) \cdot \mathbf{y}^{II}$$

where matrix **B** is defined as in (20) and

$$\mathcal{F}^{II}(\mathbf{s}; \mathbf{y}^{II}) = (\mathbf{U}\mathbf{y}^{II}) \cdot \mathbf{s}(t).$$

Thus, in the absence of external forcing terms, i.e.  $\mathcal{F}^{II}(s; y^{II}) = 0$ , and since the matrix **B** is positive definite (see Section 3), it follows that

$$\mathcal{E}_{\Upsilon}(\mathbf{y}^{II}(t^{n+1})) \le \mathcal{E}_{\Upsilon}(\mathbf{y}^{II}(t^{n})). \tag{92}$$

We also notice that, since we are not updating the variables  $\boldsymbol{u}$  and p in this step, we have  $\boldsymbol{u}^{II}(t^{n+1}) = \boldsymbol{u}^{II}(t^n)$  and  $p^{II}(t^{n+1}) = p^{II}(t^n)$ . In particular, this means that

$$\mathcal{E}_{\Omega}(\boldsymbol{u}^{II}(t^{n+1})) = \mathcal{E}_{\Omega}(\boldsymbol{u}^{II}(t^{n})), \tag{93}$$

and therefore we have that for  $n \ge 0$ 

$$\mathcal{E}_{\mathcal{O}}(\boldsymbol{u}^{II}(t^{n+1})) + \mathcal{E}_{\mathcal{T}}(\boldsymbol{y}^{II}(t^{n+1})) \le \mathcal{E}_{\mathcal{O}}(\boldsymbol{u}^{II}(t^{n})) + \mathcal{E}_{\mathcal{T}}(\boldsymbol{y}^{II}(t^{n})). \tag{94}$$

Recall that the initial conditions for Step II are the solutions of Step I, i.e.,

$$y^{II}(t^n) = y^{n+1/2} = y^I(t^{n+1}),$$
  
$$u^{II}(t^n) = u^{n+1/2} = u^I(t^{n+1}), \quad p^{II}(t^n) = p^{n+1/2} = p^I(t^{n+1}).$$

Thus combining (94) with (88) we obtain for  $n \ge 0$ 

$$\mathcal{E}_{\Omega}(\boldsymbol{u}^{II}(t^{n+1})) + \mathcal{E}_{\Upsilon}(\boldsymbol{y}^{II}(t^{n+1})) \le \mathcal{E}_{\Omega}(\boldsymbol{u}^{II}(t^{n})) + \mathcal{E}_{\Upsilon}(\boldsymbol{y}^{II}(t^{n}))$$
(95a)

$$= \mathcal{E}_{\Omega}(\boldsymbol{u}^{I}(t^{n+1})) + \mathcal{E}_{\Upsilon}(\boldsymbol{y}^{I}(t^{n+1})) \le \mathcal{E}_{\Omega}(\boldsymbol{u}^{I}(t^{n})) + \mathcal{E}_{\Upsilon}(\boldsymbol{y}^{I}(t^{n})). \tag{95b}$$

The chain of inequalities given in (95) shows that the physical energies  $\mathcal{E}_{\Omega}$  and  $\mathcal{E}_{\Upsilon}$  provide norms for the solution that, in the absence of external forcing, are bounded a priori by the initial conditions regardless of the choice of the time discretization step  $\Delta t$ , thereby concluding the proof of the theorem.

Remark 2. It is easy to show that the stability result proved in Theorem 3 also holds in the case when a Backward Euler method is used for the time discretization of both steps. However, the result provided in the theorem is more general and also holds for other time discretization methods. We also note that the theorem yields unconditional stability in the absence of external forcing. This is due to the fact that, from the physical viewpoint, if the external forces are too large the system will derange. However, the theorem could be generalized by assuming an a priori bound on the forcing terms.

# 7. Energy considerations for the functional iterations

Theorem 3 shows that the unconditional stability of the operator splitting method stems from the fact that the splitting does not disrupt the energy balance that holds at the continuous level. In particular, the interface coupling conditions are solved implicitly in Step 1 together with the Biot problem, thereby ensuring that the dissipative term in Eq. (86) associated with the resistive connection in  $\Lambda$  has a nonnegative sign.

Inspired by this result, let us now investigate the impact of the PQP and QPQ subiterations on the physical energy balance in order to get an insight into whether there may be issues associated with a potential lack of convergence. To this end, we begin by writing the energy of the time-discretized version of the fully coupled 1D-0D problem by means of the Backward Euler method (see Section 7.1), and then analyze it in the context of PQP and QPQ subiterations (see Sections 7.2 and 7.3)

## 7.1. Energy inequality for the fully coupled 1D-0D problem discretized in time via the Backward Euler method

We write the energy of the time-discretized version of the 1D-0D coupled problem by means of the Backward Euler method. Multiplying Eq. (65a) by  $(1/K)p^{n+1}$ , integrating over the interval (0, c), multiplying by the cross-sectional area ab, utilizing conditions (65b)-(65c) and the fact that  $p^{n+1}(c) = p^{n+1}$  for  $n = 0, ..., N_T - 1$ , we obtain

$$\frac{1}{K\Delta t} \|p^{n+1}\|_{L^2(\Omega)}^2 + k \|p_x^{n+1}\|_{L^2(\Omega)}^2 = \frac{ab}{K\Delta t} \int_0^c p^n p^{n+1} dx + \mathcal{F}_{\Omega}^{n+1} - Q^{n+1} P^{n+1}$$
(96)

where

$$\mathcal{F}_{\Omega}^{n+1} = \frac{ab}{K} g'(t^{n+1}) \int_{0}^{c} p^{n+1} dx.$$
 (97)

The first term on the right hand side of (96) can be bounded using Young's inequality to obtain

$$\frac{1}{2K\Delta t}\|p^{n+1}\|_{L^2(\Omega)}^2 + k\|p_x^{n+1}\|_{L^2(\Omega)}^2 \le \frac{1}{2K\Delta t}\|p^n\|_{L^2(\Omega)}^2 + \mathcal{F}_{\Omega}^{n+1} - Q^{n+1}P^{n+1}. \tag{98}$$

Defining the discrete versions of the energy and dissipation functionals for the Biot problem as:

$$\mathcal{E}_{\Omega}^{n+1} = \frac{1}{2K} \|p^{n+1}\|_{L^{2}(\Omega)}^{2} \quad \text{and} \quad \mathcal{D}_{\Omega}^{n+1} = k \|p_{x}^{n+1}\|_{L^{2}(\Omega)}^{2}, \tag{99}$$

we obtain

$$\frac{1}{\Lambda_t} \mathcal{E}_{\Omega}^{n+1} + \mathcal{D}_{\Omega}^{n+1} \le \frac{1}{\Lambda_t} \mathcal{E}_{\Omega}^n + \mathcal{F}_{\Omega}^{n+1} - Q^{n+1} P^{n+1} \tag{100}$$

which is the time-discretized version of (10) for the simplified 1D-0D problem.

Let us now consider the lumped circuit. By performing the scalar product of (70) with the vector  $\mathbf{U}\mathbf{y}^{n+1}$ , with  $\mathbf{U}$  defined in (62f), we obtain

$$\frac{1}{\Lambda t}(\mathbf{U}\mathbf{y}^{n+1}) \cdot \mathbf{y}^{n+1} + (\mathbf{B}\mathbf{y}^{n+1}) \cdot \mathbf{y}^{n+1} = \frac{1}{\Lambda t}(\mathbf{U}\mathbf{y}^{n+1}) \cdot \mathbf{y}^{n} + \mathcal{F}_{\Upsilon}^{n+1} + (\mathbf{U}\mathbf{y}^{n+1}) \cdot \mathbf{b}(Q^{n+1})$$
(101)

where  $\mathbf{B} = -\mathbf{U}\mathbf{A}$  and

$$\mathcal{F}_{\Upsilon}^{n+1} = (\mathbf{U}\mathbf{y}^{n+1}) \cdot \mathbf{s}^{n+1} . \tag{102}$$

The first term on the right hand side of (101) can be estimated by Young's inequality as follows

$$(\mathbf{U}\mathbf{y}^{n+1}) \cdot \mathbf{y}^n = (\mathbf{U}^{1/2}\mathbf{y}^{n+1}) \cdot (\mathbf{U}^{1/2}\mathbf{y}^n) \le \frac{1}{2}(\mathbf{U}^{1/2}\mathbf{y}^{n+1})^2 + \frac{1}{2}(\mathbf{U}^{1/2}\mathbf{y}^n)^2.$$

The last term on the right hand side of (101) can be rewritten utilizing the definitions of the vectors involved and the Poiseuille law at the interface to obtain

$$(\mathbf{U}\mathbf{y}^{n+1}) \cdot \mathbf{b}(Q^{n+1}) = Q^{n+1}\pi^{n+1}. \tag{103}$$

Defining the discrete versions of the energy and dissipation functionals for the circuit as:

$$\mathcal{E}_{\Upsilon}^{n+1} = \frac{1}{2} (\mathbf{U}^{1/2} \mathbf{y}^{n+1})^2 = \frac{C}{2} \left( \pi^{n+1} \right)^2 + \frac{C_1}{2} \left( \pi_1^{n+1} \right)^2 + \frac{L_1}{2} \left( Q_1^{n+1} \right)^2$$

$$\mathcal{D}_{\Upsilon}^{n+1} = (\mathbf{B} \mathbf{y}^{n+1}) \cdot \mathbf{y}^{n+1}$$

we obtain

$$\frac{1}{\Lambda_{t}}\mathcal{E}_{\Upsilon}^{n+1} + \mathcal{D}_{\Upsilon}^{n+1} \le \frac{1}{\Lambda_{t}}\mathcal{E}_{\Upsilon}^{n} + \mathcal{F}_{\Upsilon}^{n+1} + Q^{n+1}\pi^{n+1} \tag{104}$$

which is the time-discretized version of (21) for the simplified 1D-0D problem. Now, adding (100) and (104) we obtain

$$\frac{1}{\Lambda t} \left( \mathcal{E}_{\Omega}^{n+1} + \mathcal{E}_{\Upsilon}^{n+1} \right) + \mathcal{D}_{\Omega}^{n+1} + \mathcal{D}_{\Upsilon}^{n+1} \leq \frac{1}{\Lambda t} \left( \mathcal{E}_{\Omega}^{n} + \mathcal{E}_{\Upsilon}^{n} \right) + \mathcal{F}_{\Omega}^{n+1} + \mathcal{F}_{\Upsilon}^{n+1} - \mathcal{Q}^{n+1} (P^{n+1} - \pi^{n+1})$$

and, using Poiseuille's law, the last term on the right hand side can be written as

$$-Q^{n+1}(P^{n+1} - \pi^{n+1}) = -RQ^{n+1}Q^{n+1} = -R(Q^{n+1})^2 =: -\mathcal{D}_{\Lambda}^{n+1}$$
(105)

thereby providing the expected viscous dissipation associated with the resistance R in the Biot-circuit connection  $\Lambda$ . Finally, for the time-discretized 1D-0D coupled problem we can write the following energy inequality

$$\frac{1}{\Delta t} \left( \mathcal{E}_{\Omega}^{n+1} + \mathcal{E}_{\Upsilon}^{n+1} \right) + \mathcal{D}_{\Omega}^{n+1} + \mathcal{D}_{\Upsilon}^{n+1} + \mathcal{D}_{\Lambda}^{n+1} \le \frac{1}{\Delta t} \left( \mathcal{E}_{\Omega}^{n} + \mathcal{E}_{\Upsilon}^{n} \right) + \mathcal{F}_{\Omega}^{n+1} + \mathcal{F}_{\Upsilon}^{n+1} \tag{106}$$

which is the discrete counterpart of (23) for the 1D-0D coupled problem. Since all dissipative terms are nonnegative by definition, we can write

$$\frac{1}{\Lambda t} \left( \mathcal{E}_{\Omega}^{n+1} + \mathcal{E}_{\Upsilon}^{n+1} \right) \le \frac{1}{\Lambda t} \left( \mathcal{E}_{\Omega}^{n} + \mathcal{E}_{\Upsilon}^{n} \right) + \mathcal{F}_{\Omega}^{n+1} + \mathcal{F}_{\Upsilon}^{n+1} \tag{107}$$

which, in the particular case of  $\mathcal{F}_{\Omega}^{n+1} + \mathcal{F}_{\Upsilon}^{n+1} = 0$ , guarantees that the energy of the discretized system decreases as it happens at the continuous level.

We remark that, in the case of the alternative formulation (77) for the circuit, we can follow the same steps as above to obtain the following inequality for the discrete energy of the circuit

$$\frac{1}{\Delta t} \mathcal{E}_{\Upsilon}^{n+1} + \mathcal{D}_{\Upsilon}^{n+1} \leq \frac{1}{\Delta t} \mathcal{E}_{\Upsilon}^{n} + \mathcal{F}_{\Upsilon}^{n+1} + (\mathbf{U} \mathbf{y}^{n+1}) \cdot (\mathbf{V} \mathbf{y}^{n+1}) + (\mathbf{U} \mathbf{y}^{n+1}) \cdot \boldsymbol{\beta}(P^{n+1})$$

$$= \frac{1}{\Delta t} \mathcal{E}_{\Upsilon}^{n} + \mathcal{F}_{\Upsilon}^{n+1} + \frac{\pi^{n+1}}{R} \left( P^{n+1} - \pi^{n+1} \right) \tag{108}$$

which, upon utilization of Poiseuille's law and addition to the Biot part, gives the same expression as obtained in (106).

# 7.2. Energy inequality in the PQP subiterations

Within each time step  $(t^n, t^{n+1})$ , the Biot problem is solved for a given interface pressure  $P_{(j)}^{n+1}$  to update the value of the interface flow rate  $Q_{(j+1)}^{n+1}$ . As a result, the energy inequality (100) for the Biot step becomes

$$\frac{1}{\Lambda_t} \mathcal{E}_{\Omega,(j+1)}^{n+1} + \mathcal{D}_{\Omega,(j+1)}^{n+1} \le \frac{1}{\Lambda_t} \mathcal{E}_{\Omega,(j+1)}^n + \mathcal{F}_{\Omega,(j+1)}^{n+1} - Q_{(j+1)}^{n+1} P_{(j)}^{n+1}$$
(109)

The updated interface flow rate  $Q_{(j+1)}^{n+1}$  is then used to solve the circuit. As a result, the energy inequality (104) for the circuit step becomes

$$\frac{1}{\Lambda_t} \mathcal{E}_{\Upsilon,(j+1)}^{n+1} + \mathcal{D}_{\Upsilon,(j+1)}^{n+1} \le \frac{1}{\Lambda_t} \mathcal{E}_{\Upsilon,(j+1)}^{n} + \mathcal{F}_{\Upsilon,(j+1)}^{n+1} + \mathcal{Q}_{(j+1)}^{n+1} \pi_{(j+1)}^{n+1}$$
(110)

Now adding (109) and (110) we obtain the energy of the coupled system during one PQP iteration

$$\begin{split} \frac{1}{\Delta t} \left( \mathcal{E}_{\Omega,(j+1)}^{n+1} + \mathcal{E}_{\Upsilon,(j+1)}^{n+1} \right) + \mathcal{D}_{\Omega,(j+1)}^{n+1} + \mathcal{D}_{\Upsilon,(j+1)}^{n+1} &\leq \frac{1}{\Delta t} \left( \mathcal{E}_{\Omega,(j+1)}^{n} + \mathcal{E}_{\Upsilon,(j+1)}^{n} \right) \\ &+ \mathcal{F}_{\Omega,(j+1)}^{n+1} + \mathcal{F}_{\Upsilon,(j+1)}^{n+1} - \mathcal{Q}_{(j+1)}^{n+1} (P_{(j)}^{n+1} - \pi_{(j+1)}^{n+1}) \end{split}$$

For the last term on the right side of the expression above we apply Poiseuille's law and we obtain

$$-Q_{(j+1)}^{n+1}(P_{(j)}^{n+1} - \pi_{(j+1)}^{n+1}) = -Q_{(j+1)}^{n+1}(P_{(j)}^{n+1} - P_{(j+1)}^{n+1} + RQ_{(j+1)}^{n+1})$$

$$= Q_{(j+1)}^{n+1}(P_{(j+1)}^{n+1} - P_{(j)}^{n+1}) - R(Q_{(j+1)}^{n+1})^{2},$$
(111)

which is not guaranteed to provide a dissipation, as physically expected, because  $R(Q_{(j+1)}^{n+1})^2$  is nonnegative (i.e., it is a dissipation term) whereas  $Q_{(j+1)}^{n+1}(P_{(j+1)}^{n+1} - P_{(j)}^{n+1})$  does not have a definite sign. If the PQP iterations converge, then  $(P_{(j+1)}^{n+1} - P_{(j)}^{n+1}) \to 0$  as  $j \to \infty$  and the dissipative contribution is recovered despite the unphysical mismatch of the pressures at the interface. On the contrary, numerical simulations indicate that failure of PQP iterations at satisfying the convergence condition (64) is accompanied by a rapid blow-up of the term  $-Q_{(j+1)}^{n+1}(P_{(j)}^{n+1} - \pi_{(j+1)}^{n+1})$  as shown in the left panel of Fig. 10.

# 7.3. Energy inequality in the QPQ subiterations

Within each time step  $(t^n, t^{n+1})$ , the Biot problem is solved for a given interface flow rate  $Q_{(j)}^{n+1}$  to update the value of the interface pressure  $P_{(j+1)}^{n+1}$ . As a result, the energy inequality (100) for the Biot step becomes

$$\frac{1}{\Lambda_t} \mathcal{E}_{\Omega,(j+1)}^{n+1} + \mathcal{D}_{\Omega,(j+1)}^{n+1} \le \frac{1}{\Lambda_t} \mathcal{E}_{\Omega,(j+1)}^{n} + \mathcal{F}_{\Omega,(j+1)}^{n+1} - Q_{(j)}^{n+1} P_{(j+1)}^{n+1}$$
(112)

The updated interface pressure  $P_{(j+1)}^{n+1}$  is then used to solve the circuit. As a result, the energy inequality (108) for the circuit step becomes

$$\frac{1}{\Delta t} \mathcal{E}_{\Upsilon,(j+1)}^{n+1} + \mathcal{D}_{\Upsilon,(j+1)}^{n+1} \le \frac{1}{\Delta t} \mathcal{E}_{\Upsilon,(j+1)}^{n} + \mathcal{F}_{\Upsilon,(j+1)}^{n+1} + \frac{\pi_{(j+1)}^{n+1}}{R} \left( P_{(j+1)}^{n+1} - \pi_{(j+1)}^{n+1} \right) \tag{113}$$

Now adding (112) and (113) we obtain the energy of the coupled system during one QPQ iteration

$$\begin{split} \frac{1}{\Delta t} \left( \mathcal{E}_{\Omega,(j+1)}^{n+1} + \mathcal{E}_{\Upsilon,(j+1)}^{n+1} \right) + \mathcal{D}_{\Omega,(j+1)}^{n+1} + \mathcal{D}_{\Upsilon,(j+1)}^{n+1} &\leq \frac{1}{\Delta t} \left( \mathcal{E}_{\Omega,(j+1)}^{n} + \mathcal{E}_{\Upsilon,(j+1)}^{n} \right) \\ &+ \mathcal{F}_{\Omega,(j+1)}^{n+1} + \mathcal{F}_{\Upsilon,(j+1)}^{n+1} - Q_{(j)}^{n+1} P_{(j+1)}^{n+1} + \frac{\pi_{(j+1)}^{n+1}}{R} \left( P_{(j+1)}^{n+1} - \pi_{(j+1)}^{n+1} \right) \end{split}$$

Let us consider the last two terms on the right side of the expression above. When applying Poiseuille's law we now obtain

$$-Q_{(j)}^{n+1}P_{(j+1)}^{n+1} + \frac{\pi_{(j+1)}^{n+1}}{R} \left( P_{(j+1)}^{n+1} - \pi_{(j+1)}^{n+1} \right) = -Q_{(j)}^{n+1}P_{(j+1)}^{n+1} + Q_{(j+1)}^{n+1}\pi_{(j+1)}^{n+1}$$

$$= P_{(j+1)}^{n+1}(Q_{(j+1)}^{n+1} - Q_{(j)}^{n+1}) - R(Q_{(j+1)}^{n+1})^{2},$$
(114)

which is not guaranteed to provide a dissipation, as physically expected, because  $R(Q_{(j+1)}^{n+1})^2$  is nonnegative (i.e., it is a dissipation term) whereas  $P_{(j+1)}^{n+1}(Q_{(j+1)}^{n+1}-Q_{(j)}^{n+1})$  does not have a definite sign. If the QPQ iterations converge, then  $(Q_{(j+1)}^{n+1}-Q_{(j)}^{n+1})\to 0$  as  $j\to\infty$  and the dissipative contribution is recovered despite the unphysical mismatch of the flow rates at the interface. On the contrary, numerical simulations indicate that failure of QPQ iterations at satisfying the convergence condition (76) is accompanied by a rapid blow-up of the term  $-Q_{(j)}^{n+1}P_{(j+1)}^{n+1}+\pi_{(j+1)}^{n+1}(P_{(j+1)}^{n+1}-\pi_{(j+1)}^{n+1})/R$  as shown in the right panel of Fig. 10.

#### 8. Numerical results

In this section we compare the performance of the PQP and QPQ subiterations and operator splitting method in the numerical simulation of the coupled Biot-circuit problem. We first study the 1D-0D example considered in Section 5, showing that the obtained results are in good agreement with the analytical solution illustrated in Appendix I (see Section 8.1). Then, we demonstrate in Section 8.2 the potentiality of the proposed methods to treat multidimensional coupled Biot-circuit systems. To this purpose, we first consider in Section 8.2.1 the 3D version of the 1D-0D formulation, showing that the obtained results are in agreement with those reported in Section 8.1. Then, we illustrate in Section 8.2.2 the simulation of a 3D-0D coupled problem where the solution of the Biot subsystem does not exhibit any spatial symmetry, showing how also in this case the proposed solution methods are capable of enforcing the boundary condition (7) on  $\Sigma$  and maintain the properties of stability and accuracy exhibited in the previous tests.

## 8.1. Simulation of the 1D-0D Biot coupled system with analytical solution

We consider the case where f, S, and g are equal to zero and the model parameters are equal to the values reported in Table 2. The derivation of the exact solution of the system is illustrated in Appendix I. The main aim of the analysis is to investigate, given physical and geometrical parameters of the system, how the choice of  $\Delta t$  may affect accuracy, convergence and stability of the proposed solution methods. For each of the three considered algorithms, we have adopted the following choices regarding the discretization methods:

- 1. temporal discretization of Biot and circuit problems is conducted using the Backward Euler method with a uniform time step  $\Delta t$ ;
- 2. spatial discretization of the Biot problem is conducted using the finite element method with piecewise linear continuous elements for the approximation of the solid displacement u and the fluid pressure p on a uniform partition of (0, c) made of  $M_h$  elements of size  $h = c/M_h$ .

The values of  $M_h$  and  $\Delta t$  adopted in the numerical simulations are shown in Table 1. The table also reports the number of terms  $N_{\text{terms}}$  used to evaluate the series expansions and the number of elements  $M_{\text{int}}$  used to evaluate the integrals between 0 and t with the trapezoidal quadrature rule that are needed to compute the exact solution described in Section 5.

Parameter	Description	Value
$M_h$	# of intervals for spatial discretization	100
$\Delta t$	Time step	$10^{-1}, 2 \cdot 10^{-2}$
$N_{ m terms}$	# of terms evaluated in the series of the exact solution	100
$M_{ m int}$	# of elements for the numerical integration on $[0, t]$	100

Table 1: Discretization parameters used in the simulations.

For the PQP fixed-point method, subiterations are stopped as soon as the relative distance between  $P_{(j+1)}$  and  $P_{(j)}$  falls below  $tol_P = 10^{-15}$ . Instead, for the QPQ fixed-point method, subiterations are stopped as soon as the absolute distance between  $Q_{(j+1)}$  and  $Q_{(j)}$  falls below  $tol_Q = 10^{-15}$ , but similar results are obtained by controlling their relative distance (not shown in this paper). In each case, the maximum number of iterations is set to 100.

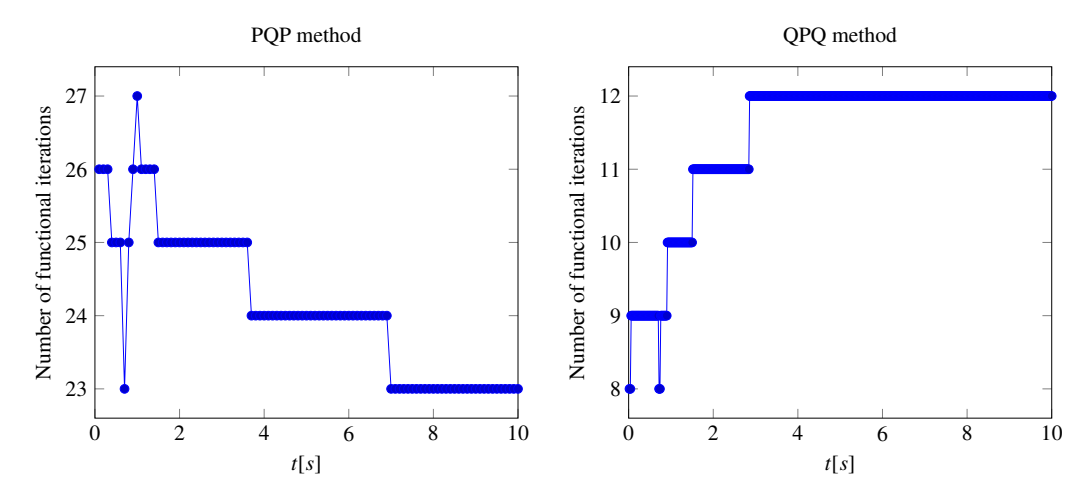


Fig. 9: Left: convergence history of the PQP subiterations for  $\Delta t = 0.1s$ . Right: convergence history of the QPQ subiterations for  $\Delta t = 0.02s$ .

# 8.1.1. Convergence and stability of the PQP and QPQ subiterations

We run experiments for two different values of the time discretization parameter, namely  $\Delta t_1 = 0.1s$  and  $\Delta t_2 = 0.02s$ . While the operator splitting method is always stable regardless of the choice of  $\Delta t$ , the convergence of the PQP and QPQ iterations may not be ensured. Specifically, Fig. 7 and Fig. 8 show that  $|\gamma_2(\Delta t_1)| < 1$  and  $|\alpha_2(\Delta t_1)| > 1$ , whereas  $|\gamma_2(\Delta t_2)| > 1$  and  $|\alpha_2(\Delta t_2)| < 1$ . Thus, the sufficient conditions in Theorems 1 and 2 guarantee convergence of the PQP subiterations for  $\Delta t_1$  but not for  $\Delta t_2$ . Conversely, convergence of the QPQ subiterations is guaranteed for  $\Delta t_2$  but not for  $\Delta t_1$ .

Fig. 9 shows the convergence history of the PQP and QPQ methods in the cases where the sufficient conditions are satisfied. Results indicate that the number of iterations required for any of the two fixed-point methods to converge at each time level does not exceed 27 for the PQP iterations and 12 for the QPQ iterations. It is worth noticing that the actual number of functional iterations required by the PQP and QPQ fixed-point methods at each time level may:

- vary depending on the time level, since the change in the solution may not be uniform with respect to time. In this regard, choosing the time step in an adaptive way may help, but it may not be straightforward due to the non-monotonic behavior of  $|\gamma_2(\Delta t)|$  and  $|\alpha_2(\Delta t)|$ ;
- vary depending on the specific value chosen for the tolerances;
- vary depending on whether the relative or absolute distance is used for the convergence criterium.

To better investigate how the convergence of the PQP and QPQ subiterations depend on  $\Delta t$ , we show in Fig. 10 the time evolution of the term  $-Q_{(j+1)}^{n+1}(P_{(j)}^{n+1}-\pi_{(j+1)}^{n+1})$  in Eq. (111) and the term  $-Q_{(j)}^{n+1}P_{(j+1)}^{n+1}+\pi_{(j+1)}^{n+1}\left(P_{(j+1)}^{n+1}-\pi_{(j+1)}^{n+1}\right)/R$  in Eq. (114) for the choices of  $\Delta t$  when convergence is not guaranteed. We note that these terms have the physical units of a power, namely Watt (W), with W = Kg m<sup>2</sup> s<sup>-3</sup>. We remark that these terms are on the right hand side of the energy balance, thereby providing a dissipation if they are nonpositive.

Results show that, when the sufficient condition for convergence is not verified, the terms in Eq. (111) and Eq. (114) become positive, instead of being negative as required by the physics of dissipative mechanisms. Furthermore, these terms blow-up resulting in machine overflow. These results confirm that the lack of convergence of the PQP and QPQ iterations is associated with a disruption of the physics embodied in the interface conditions.

#### 8.1.2. Accuracy of the PQP and QPO subiterations compared to the Operator Splitting method

Fig. 11 shows a comparison between the exact circuit variables and their numerical approximations obtained with the PQP and operator splitting methods for  $\Delta t = 0.1s$ . A close inspection of the plots of P, Q and  $Q_1$  reveals that the PQP subiterations provide a more accurate solution than the operator splitting method at the price, however, of a higher computational cost.

Fig. 12 shows a comparison between the exact circuit variables and their numerical approximations obtained with the QPQ and operator splitting methods for  $\Delta t = 0.02s$ . Results indicate that QPQ and operator splitting methods

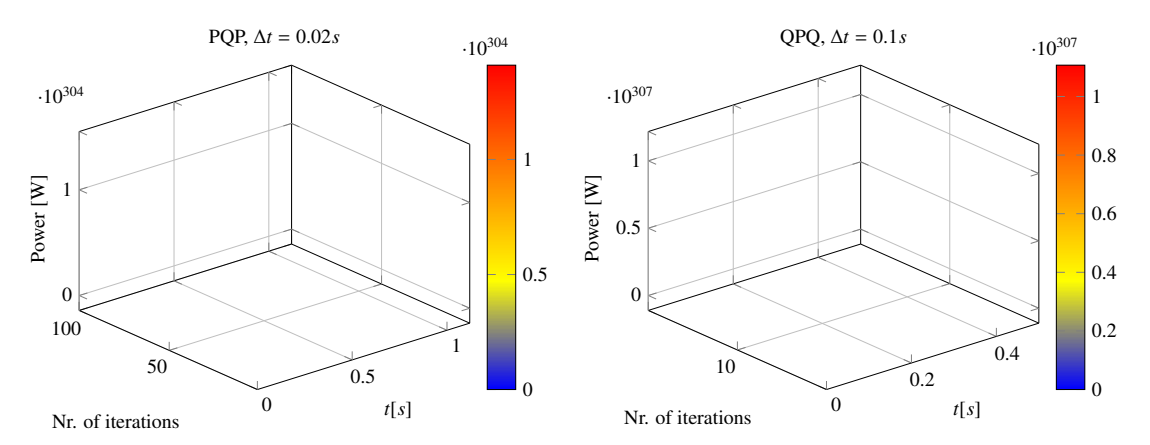


Fig. 10: Left: Plot of the term  $-Q_{(j+1)}^{n+1}(P_{(j)}^{n+1} - \pi_{(j+1)}^{n+1})$  in Eq. (111) for  $\Delta t = 0.02s$ , when the sufficient condition for the convergence of the PQP subiterations is not satisfied. Right: Plot of the term  $-Q_{(j)}^{n+1}P_{(j+1)}^{n+1} + \pi_{(j+1)}^{n+1}(P_{(j+1)}^{n+1} - \pi_{(j+1)}^{n+1})/R$  in Eq. (114) for  $\Delta t = 0.1s$ , when the sufficient condition for the convergence of the QPQ subiterations is not satisfied.

provide solutions of similar (good) accuracy except in the case of the variables Q and  $Q_1$ , for which the QPQ fixed-point method fails to provide an accurate computation. The inaccurate evaluation of Q and  $Q_1$  may be ascribed to the combination of Q in the reduced coercivity of the boundary value problem for solid displacement and fluid pressure associated with Neumann boundary conditions at both endpoints of the Biot domain, and Q in the round-off error arising from cancellation problems in evaluating the difference between Q and Q (see Eq. Q).

Fig. 13 shows a comparison between the exact energy functional  $\mathcal{E}(t) = \mathcal{E}_{\Omega}(t) + \mathcal{E}_{T}(t)$  and its numerical approximations computed with the PQP, QPQ, and operator splitting methods for  $\Delta t = 0.1s$  and  $\Delta t = 0.02s$ . We remark that the physical units of energy is Joule (J), with  $J = Kg m^2 s^{-2}$ . In the case  $\Delta t = 0.1s$ , the sufficient condition for convergence is satisfied by the PQP subiterations but not for the QPQ subiterations. Interestingly, the PQP method computes an accurate approximation of the energy, whereas the approximation computed by the QPQ method blows up at the first time level, t = 0.1s. In the case  $\Delta t = 0.02s$ , the situation reverses as now the sufficient condition for convergence is satisfied only in the case of the QPQ iterations. Interestingly, the approximation computed by the PQP method blows up at t = 0.06s, whereas the QPQ method computes an accurate approximation of the energy. Remarkably, for each value of  $\Delta t$ , the operator splitting method is stable and computes an accurate approximate energy.

# 8.2. Simulation of the 3D-0D Biot-circuit problem

In this section we implement the solution methods proposed in this article to numerically approximate the coupled Biot-circuit system in the case where the computational domain  $\Omega$  is a three-dimensional open bounded subset of  $\mathbb{R}^3$ . For the spatial discretization of the 3D part of the coupled system, we propose a Hybridized Discontinuous Galerkin method (HDG), which has several attractive features: i) it provides optimal approximation of both primal and flux variables; ii) it requires less globally coupled degrees of freedom than DG methods of comparable accuracy; iii) it naturally handles integral boundary conditions (IBCs). Well-posedness analysis of a Poisson model problem equipped with IBCs has been addressed in [66] and can be easily extended to system (129). In the presence of an integral boundary condition on a given portion of  $\partial\Omega$ , the scalar solution of the Poisson problem is required to be equal to an (unknown) constant on that portion of  $\partial\Omega$  [66]. Details about the HDG discretization and its implementation for the PQP and QPQ subiterations and for the operator splitting algorithm are given in Appendix II. Discontinuous finite elements of degree 1 are employed in all the numerical experiments illustrated in the remainder of the section. The three-dimensional computational domain analyzed in Section 8.2.1 is discretized with a fully unstructured grid made of 1577 tetrahedra whereas in the test case studied in Section 8.2.2 a finer unstructured grid with 97806 tetrahedra is used.

#### 8.2.1. Simulation of the 3D-0D Biot coupled system with one-dimensional solution

We begin by considering the 3D-0D problem that led to the 1D-0D example introduced in Section 5. Snapshots of the 3D fields obtained as a solution of the 3D-0D coupled problem via operator splitting are reported in Fig. 14. Results closely agree with those obtained by solving the same problem in the 1D-0D case in Section 8.1. In particular,

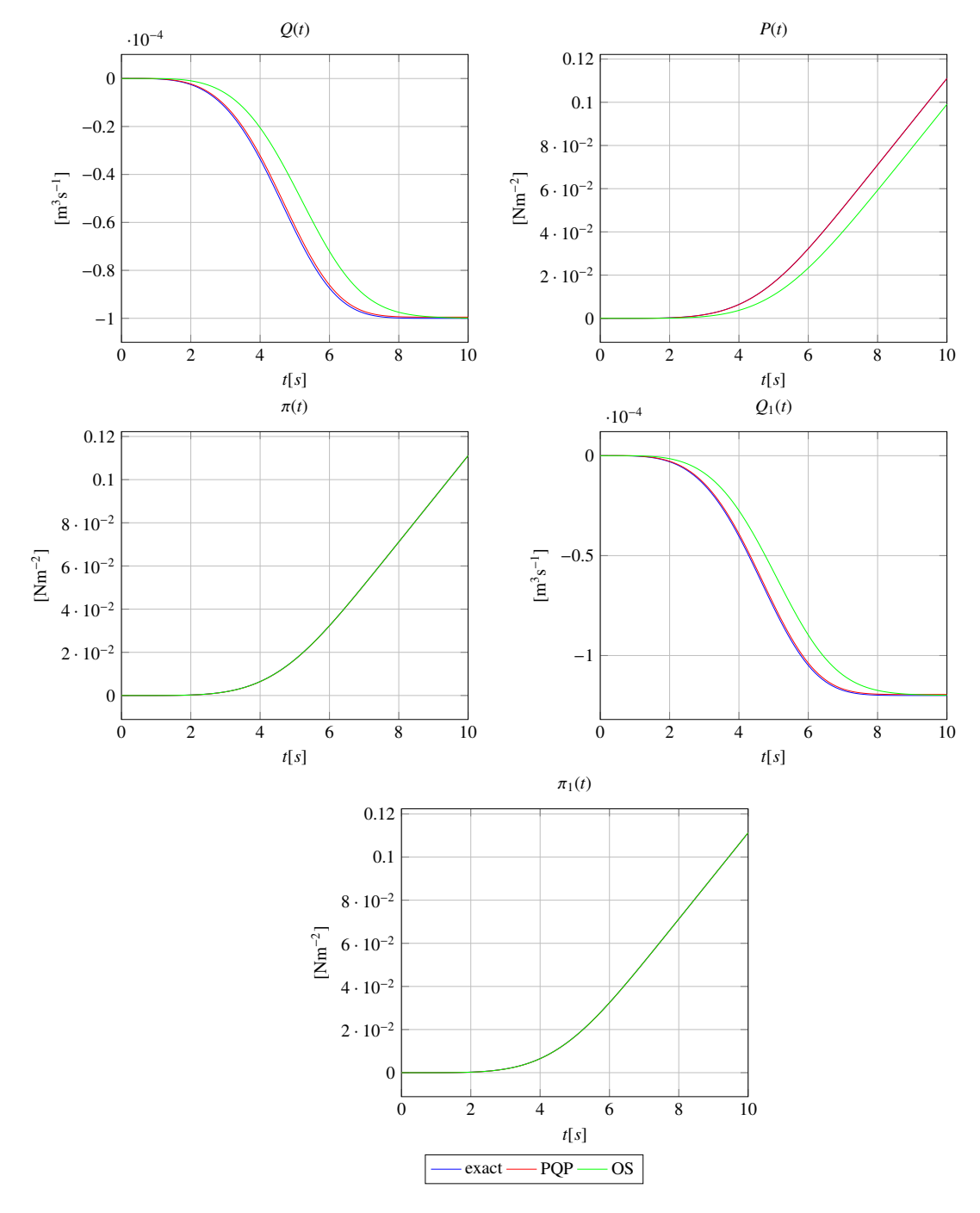


Fig. 11: Comparison between the exact circuit variables and their numerical approximations obtained with the PQP and operator splitting (OS) methods for  $\Delta t = 0.1 s$ .

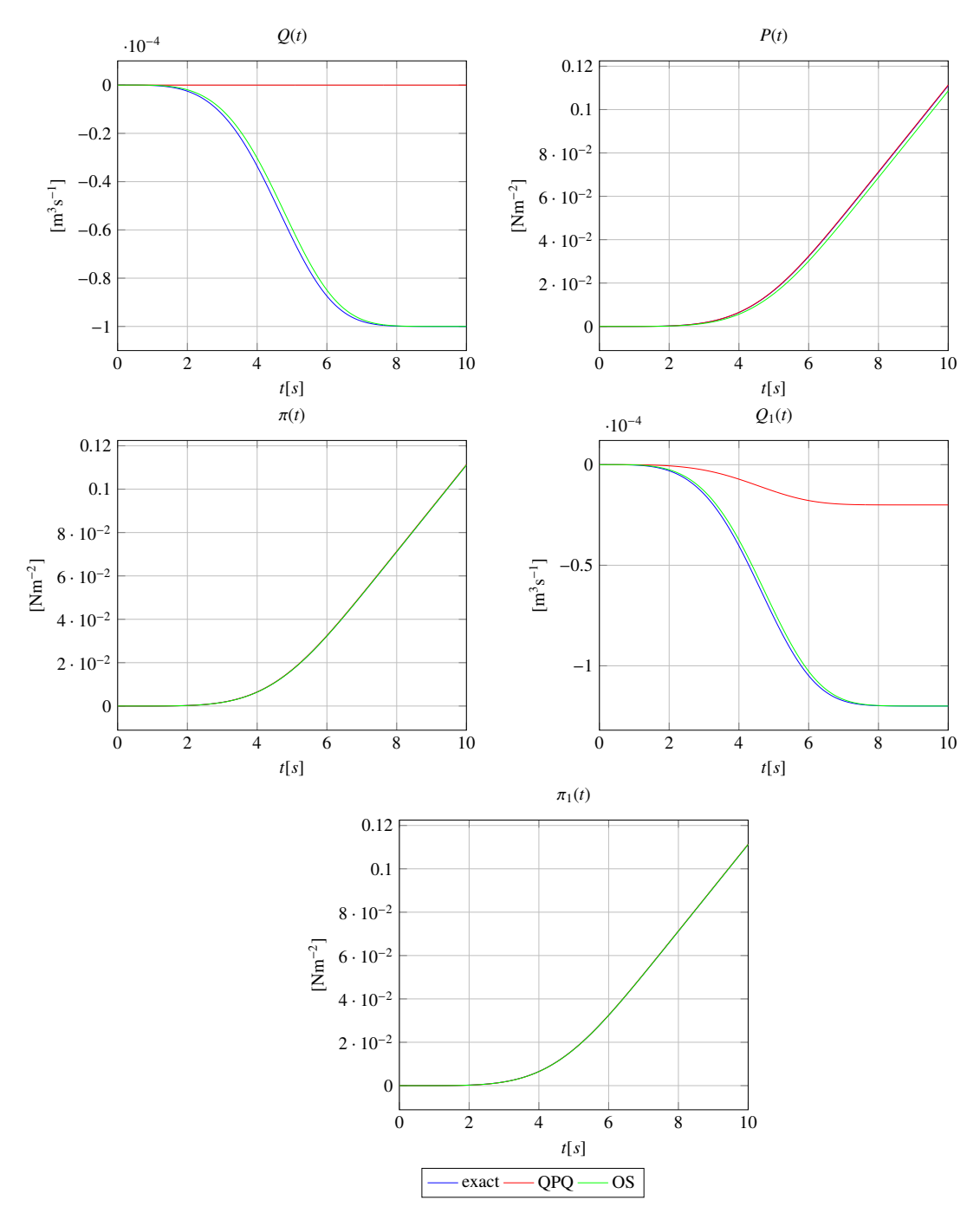


Fig. 12: Comparison between the exact circuit variables and their numerical approximations obtained with the QPQ and operator splitting (OS) methods for  $\Delta t = 0.02s$ .

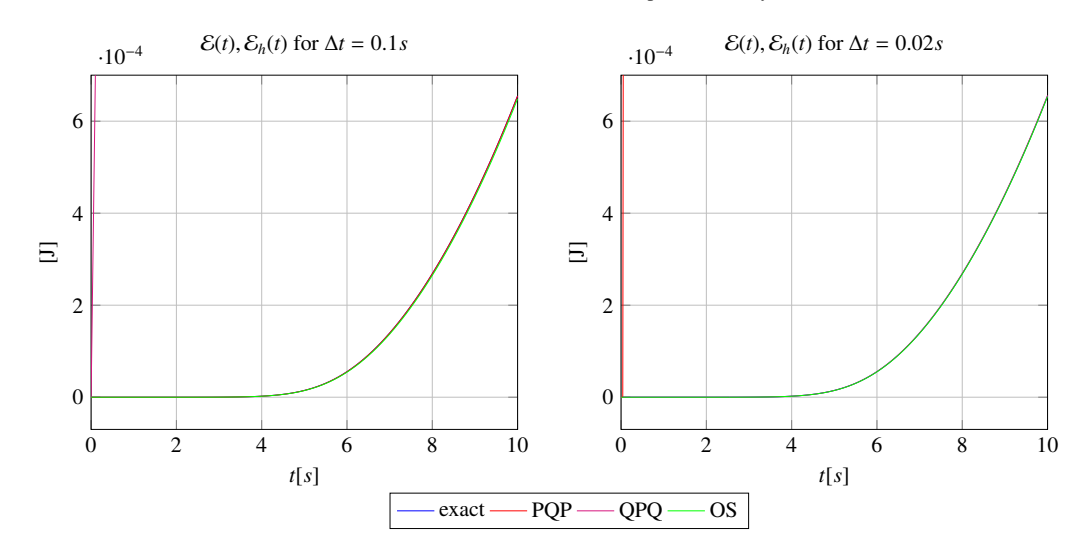


Fig. 13: Comparison between the exact energy function  $\mathcal{E}(t) = \mathcal{E}_{\Omega}(t) + \mathcal{E}_{T}(t)$  and its numerical approximations computed with the PQP, QPQ and operator splitting (OS) methods. *Left*:  $\Delta t = 0.1s$ . *Right*:  $\Delta t = 0.02s$ .

we see how the pressure varies only along the axis of the parallelepiped, and that also the velocity and displacement fields are unidirectional.

A comment is in order to justify the added value of the above results with respect to those obtained in Section 8.1. As a matter of fact, despite the 3D-0D problem treated in the present section has the same mathematical solution as the 1D-0D problem, the computational algorithm to determine the spatial distributions of the dependent variables of the Biot subsystem is based on a fully unstructured geometrical discretization of the parallelepiped shown in Fig. 5 which does not take advantage of the one-dimensional nature of the problem, thereby making the verification of the correct outcome of the 3D-0D simulation a nontrivial check. It is well-known, indeed, that finite element computations on unstructured grids may give rise to undesired mesh-orientation effects which are not occurring with the HDG formulation utilized in our numerical solver (see, e.g., [67] in the case of advection-diffusion equations and [68] in the case of structural mechanics).

#### 8.2.2. Simulation of the 3D-0D Biot coupled system with a three-dimensional solution

In this section we consider the same computational domain as in Section 8.2.1, but we adopt the following different set of boundary conditions:

$$\mathbf{T} \boldsymbol{n} = \boldsymbol{0},$$
  $\mathbf{K}^{1/2} \tilde{\boldsymbol{v}} \cdot \boldsymbol{n} = 0,$  on  $\Gamma_N \times (0, T),$   $\boldsymbol{u} = \boldsymbol{0},$   $\mathbf{K}^{1/2} \tilde{\boldsymbol{v}} \cdot \boldsymbol{n} = \psi,$  on  $\Gamma_{D,v} \times (0, T),$ 

with:

$$\Gamma_N = \{ x \in \partial \Omega \mid y = 0.05 \text{ or } z = -0.05 \text{ or } z = 0.05 \},$$
  
 $\Gamma_{D,v} = \{ x \in \partial \Omega \mid x = 0 \text{ or } y = -0.05 \},$ 

and

$$\psi(x, y, z) = \begin{cases} -0.2\cos(10\pi y)\cos(10\pi z)(1 + 0.5\cos(0.2\pi t)) & \text{for } x = 0, \\ 0.2e^{-1000*((x - 0.45)^2 + z^2)}(1 - 0.5\sin(0.3\pi t)) & \text{for } y = -0.05. \end{cases}$$

We also let  $\Gamma_{D,p} = \Gamma_0 = \emptyset$ , and impose on  $\Sigma = \{x \in \partial\Omega \mid x = 0.5\}$  the same integral boundary condition as in Section 8.2.1. The above choice of the boundary conditions gives rise to a solution that, unlike the case studied in Section 8.2.1, does not exhibit any spatial symmetric behavior. In particular, the Gaussian form of the function  $\psi$  at y = -0.05 is meant to simulate the localized presence at x = 0.45 of a leakage fluid flow.

Snapshots of the solutions at the final time level  $t = T_{\text{end}}$  obtained with the operator splitting method for  $\Delta t = 0.1$ s are shown in Figures 15, 16 and 17.

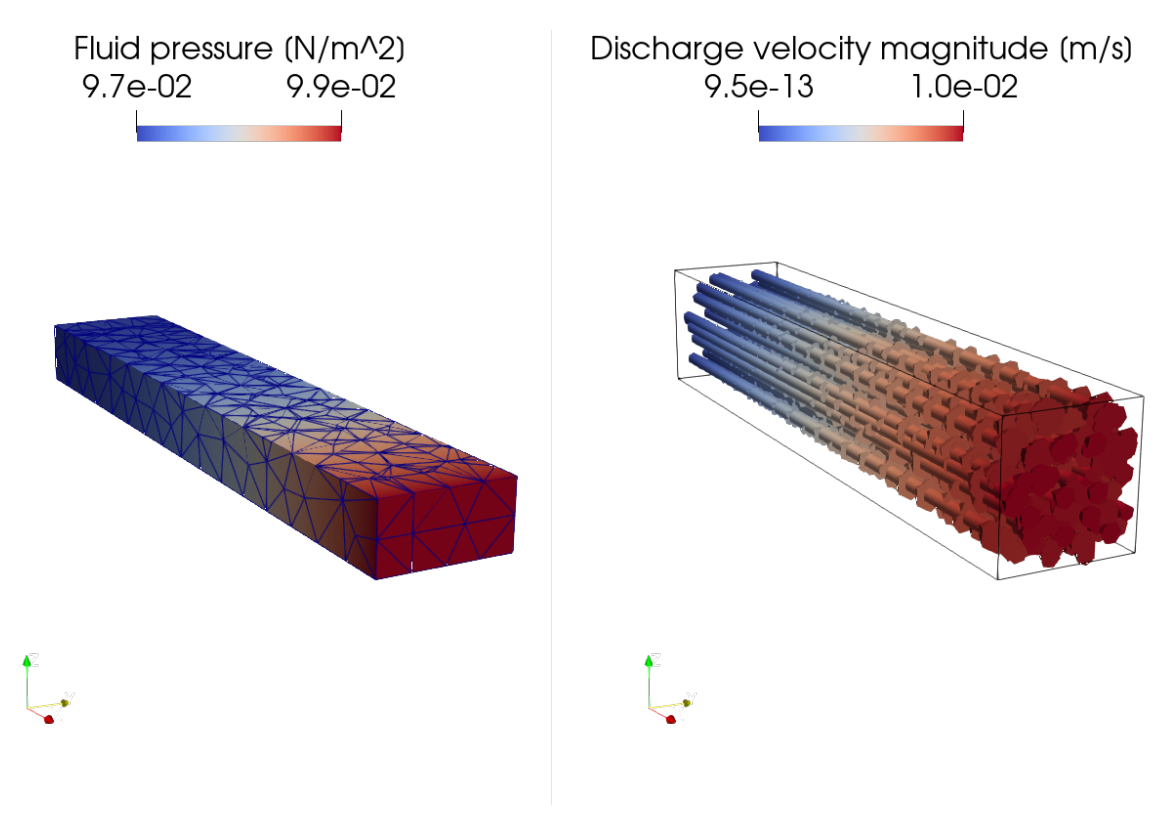
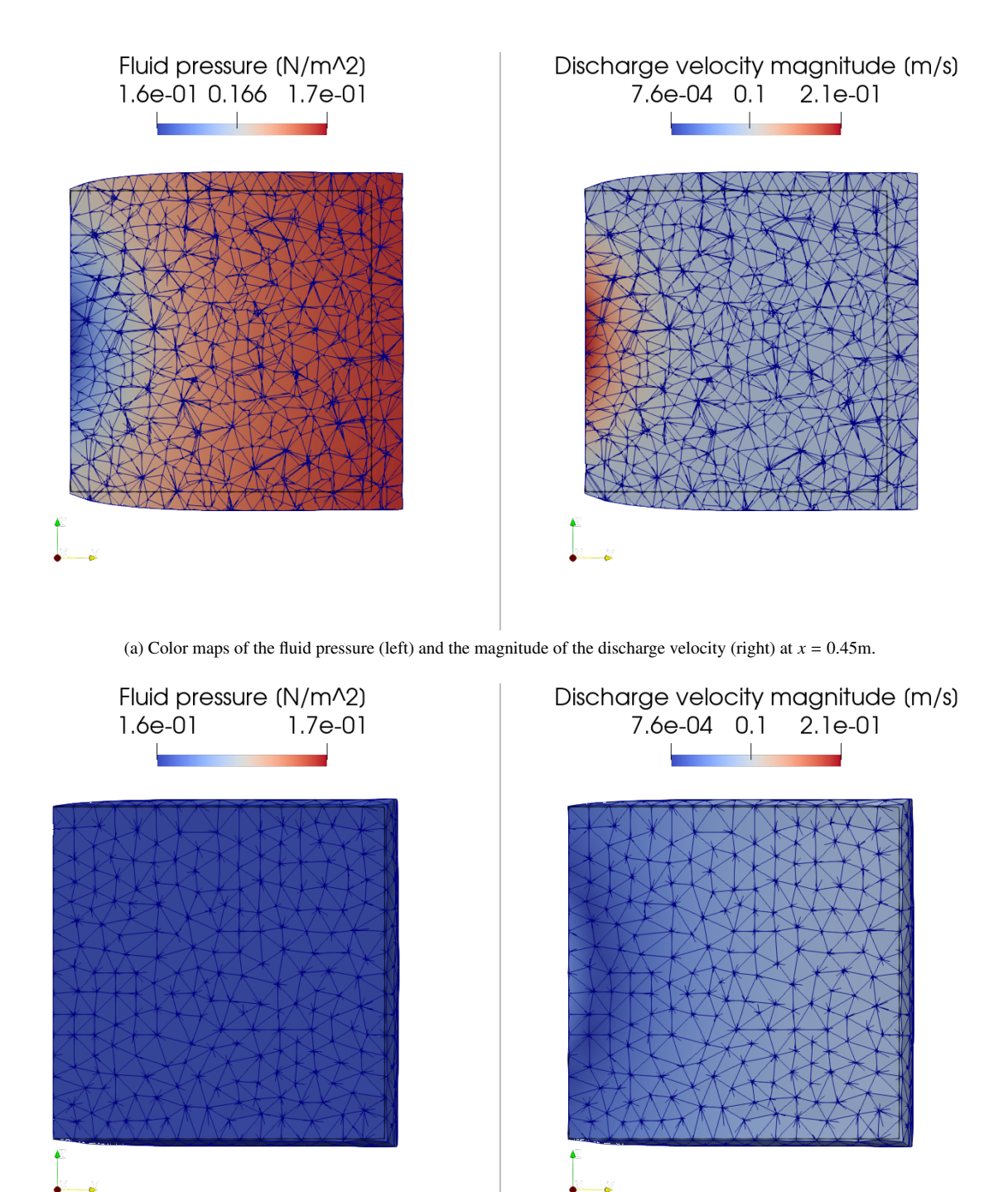


Fig. 14: Simulation of a 3D-0D coupled Biot-circuit system with a one-dimensional solution. Plot of the approximate Biot variables at t = 10 s obtained with the operator splitting (OS) method for  $\Delta t = 0.10$  s. Specifically, pressure (top, left), velocity (top, right) and displacement (bottom) are displayed. In (c), the initial configuration (white wireframe) is reported along with the deformed configuration (blue wireframe).



(b) Color maps of the fluid pressure (left) and the magnitude of the discharge velocity (right) at x = 0.5m.

Fig. 15: Simulation of a 3D-0D coupled Biot-circuit system with a three-dimensional solution. Color maps of the approximate fluid pressure and discharge velocity at x = 0.45m and at the interface  $\Sigma$  (x = 0.5m), on the deformed configuration at the final time level  $t = T_{\text{end}}$ . The initial configuration is shown by the black outline.

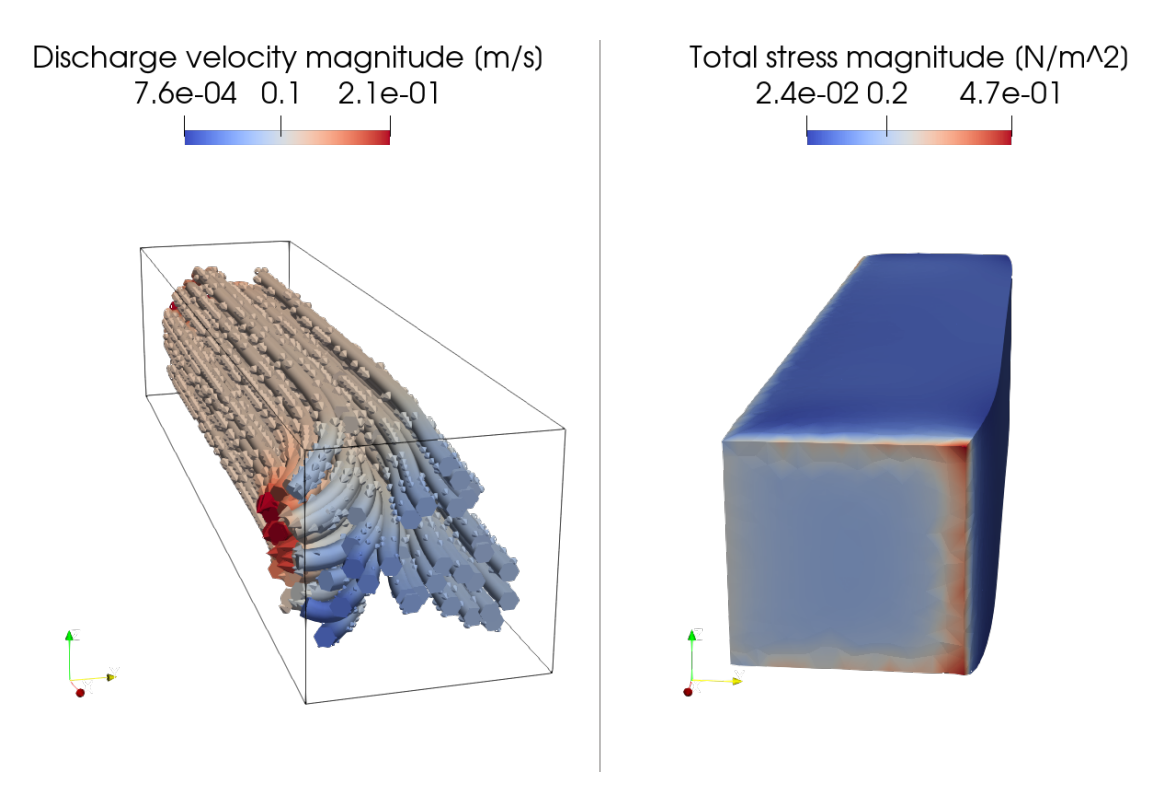


Fig. 16: Simulation of a 3D-0D coupled Biot-circuit system with a three-dimensional solution. Streamlines of the discharge velocity  $\tilde{v}_h$  and magnitude of the total stress  $T_h$  on the deformed configuration at the final time level  $t = T_{\text{end}}$ .

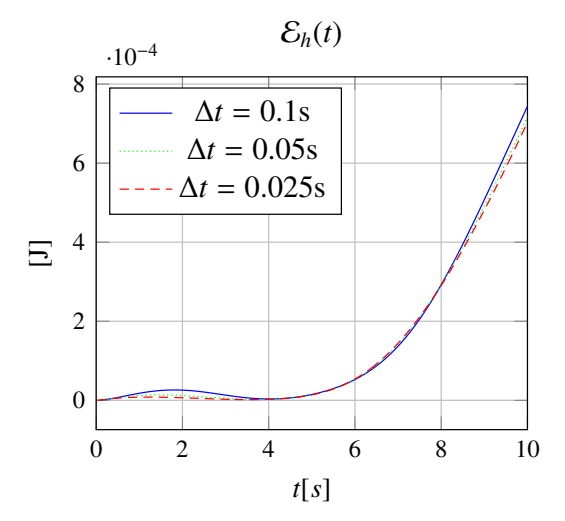


Fig. 17: Simulation of a 3D-0D coupled Biot-circuit system with a three-dimensional solution. Numerical approximations of the energy function  $\mathcal{E}_h(t) = \mathcal{E}_{h,\Omega}(t) + \mathcal{E}_{h,\Upsilon}(t)$  computed with operator splitting (OS) method for decreasing values of the time step  $\Delta t$ .

The color plots in the top panel of Fig. 15 indicate the presence of a leakage fluid flow at x = 0.45m. In particular, we see the presence of an horizontal gradient from right to left in the pressure color plot (top panel, left) which determines the nonuniform distribution of velocity magnitude illustrated in the right side of the top panel, Fig. 15 shows also the ability of the integral boundary condition to comply with the conservation of mass requirement at the 3D-0D coupling, despite the flow leakage at x = 0.45m.

The color plots in the bottom panel of Fig. 15 demonstrate the ability of the operator splitting method, combined with the HDG discretization, in describing a spatially nonuniform velocity over the interface  $\Sigma$  at x = 0.5m (bottom panel, right) while computing at the same time a spatially constant pressure (bottom panel, left), unlike what happens in Section 8.2.1.

The vector plot in the left panel of Fig. 16 represents the streamlines of the discharge velocity  $\tilde{v}_h$  at the final time level  $t = T_{\text{end}}$  and confirm that the fluid flow is far from being spatially uniform throughout the computational domain, especially in the proximity of the outlet section at x = 0.5m.

The color plot in the right panel of Fig. 16 represents the magnitude of the total stress  $\mathbf{T}_h$  on the deformed configuration at the final time level  $t = T_{\text{end}}$ . In particular, we see that the total stress magnitude increases from left to right and, consistently, the solid material exhibits a larger deformation on the right side of the parallelepiped.

Finally, Fig. 17 illustrates the time evolution of the total energy function computed by the operator splitting method in combination with the HDG discretization as a function of the time step  $\Delta t$ . We see that the slightly "wavy" shape of the energy occurring for a larger value of  $\Delta t$  tends to vanish as  $\Delta t$  becomes smaller. At the same time, we see that no blow-up occurs as time increases, for any value of the time discretization parameter, thus confirming the unconditional stability of the operator splitting approach.

# 9. Conclusions and future developments

The present work studies and compares numerical strategies for the solution of a PDE-ODE coupled system representing the flow of a fluid through a poroelastic medium connected with a lumped hydraulic circuit. This multiscale coupling leads to interface conditions enforcing the continuity of mass and the balance of stresses across different scales, and this constitutes the main challenge in the numerical solution of the problem.

Starting from the continuous level in space, we have formulated two algorithms that compute the problem dependent variables through a partition of the time interval into a finite number of subintervals of uniform width  $\Delta t$ . The first solution approach is based on functional iterations, specifically PQP and QPQ subiterations, whereas the second approach is based on the operator splitting method.

The main conclusion of our theoretical and computational investigation is that it is not possible, as it is often the case in Numerical Analysis, to neatly identify whether a formulation is definitely superior to the other because both have advantages and disadvantages.

Specifically, operator splitting does not require any subiteration step during the advancement from the discrete time level  $t^n$  to the discrete time level  $t^{n+1}$ , so that its computational cost basically depends on the product of the number of degrees of freedom for space discretization times the number of discrete time levels. On the contrary, PQP and QPQ subiterations are subject to certain conditions to properly function, which are related to the contractivity property of the associated fixed-point map, and these conditions depend nonlinearly on model parameters and  $\Delta t$ . Therefore, the amount of computational resources needed by the functional iteration approach cannot be predicted before hand since it heavily depends on the interplay between convergence conditions and convergence criteria used to terminate the iteration process. This aspect may be particularly cumbersome when dealing with problems in multiple spatial dimensions.

Interestingly, when functional iterations fail to converge, results show that the solution blows up and the problem cannot be simply solved by reducing  $\Delta t$  (which would be the most natural remedy) because the dependence of the contractivity constant on  $\Delta t$  is nonmonotone. This problem does not arise in the operator splitting method thanks to its unconditional stability with respect to  $\Delta t$ . However, when the functional iterations converge, results suggest that the PQP subiterations provide a solution characterized by a better time accuracy when compared with the operator splitting method, given the same number of spatial and temporal degrees of freedom. We note that each considered solution approach could be made more sophisticated than examined in this article by introducing, for example, a relaxation parameter in the functional iterations or symmetrization in the operator splitting method. These improvements go beyond the scope of this paper, which aims at unveiling the fundamental differences between the two approaches.

In this perspective, an important aspect that we have thoroughly analyzed in this work is related to how the proposed methods are able to preserve at the discrete level the energy balance that is verified by the coupled PDE-

ODE system at the continuous level. Our theoretical analysis shows that in the absence of external source terms, the operator splitting method ensures that the total energy stored in the system is a decreasing function of time, this property being due to the fact that the dissipative term associated with the resistive connection between the Biot part of the system and the lumped circuit maintains a definite sign during the simulations. On the contrary, functional iterations fail in general to ensure a-priori that the above mentioned dissipative term has a definite sign, because they introduce a spurious contribution which can be seen to tend to zero or blow up depending on the fact that the iterations succeed or fail to satisfy the contractivity convergence condition. This spurious contribution is due to the fact that, in the functional iterations, the interface conditions are decoupled in two separate steps, thereby disrupting the energy balance at the interface. Conversely, the operator splitting method solves the interface conditions implicitly together with the PDE subproblem, thereby preventing artificial disruptions of the interface energy balance.

Based on this markedly different behavior of the two proposed solution approaches, as far as energy conservation is concerned, the operator splitting method appears to be a promising technique for a physically sound and robust treatment of several other applications in applied sciences characterized by the mathematical modeling of coupled multiscale systems. In addition to fluid flow through complex systems, other applications may include the design and simulation of integrated circuits (ICs) in nanoelectronics in which the PDE part of the model is typically devoted to the detailed study of the microscopic properties of a single component of the IC, whereas the electric lumped parameter circuit part of the model describes the remainder of the IC.

# Acknowledgements

This work has been partially supported by NSF-CAREER 1555062 (L. Bociu), NSF-DMS 1853222/2021192 (G. Guidoboni) and NSF-DMS 2108711/2108665 (Bociu/Guidoboni).

# Appendix I: analytical solution of the 1D-0D example of coupled Biot-circuit system

In this section we illustrate how to reformulate the 1D Biot model introduced in Section 5 so that an analytical expression for its solution can be derived. Then, we exhibit a particular solution that is used to assess the performance of the numerical schemes investigated in this work.

**Reformulation of the 1D Biot model**. Let us consider the special case in which the volumetric sources S and f in Eqs. (59a) and (59b) are equal to zero. Furthermore, let us denote by  $\phi_x$  the partial derivative of  $\phi$  with respect to x for any function  $\phi$ :  $[0, c] \times \mathbb{R}$  such that  $(x, t) \to \phi(x, t)$ . In this case, the 1D Biot model (59) can be reformulated as the following parabolic system for the pressure variable p (see [28]):

$$\begin{cases} p_{t} - kKp_{xx} = g'(t), & x \in (0, c), t \in (0, T) \\ p_{x}(0, t) = 0, & t \in (0, T) \\ p_{x}(c, t) = -\frac{Q(t)}{kab}, & t \in (0, T) \\ p(x, 0) = p_{0}(x), & x \in (0, c) \end{cases}$$
(115)

where g'(t) is the time derivative of g = g(t) and  $p_0(x) = Ku_x(x, 0) + g(0) = K\chi_x(x) + g(0)$ . We note here that once we solve (115) for p(x, t), we can recover the elastic displacement u(x, t) from the following relations:

$$u_x(x,t) = \frac{1}{K} (p(x,t) - g(t))$$
 and  $u(c,t) = 0$ .

In order to solve (115), we first homogenize the boundary conditions. To this end, we introduce the auxiliary dependent variable

$$\widehat{p}(x,t) = p(x,t) + \frac{Q(t)}{kab} \left[ x + \frac{1}{2c} (x - c)^2 \right]$$
(116)

and note that  $\widehat{p}$  satisfies the following heat equation with homogeneous Neumann boundary conditions:

$$\begin{cases} \widehat{p}_{t} - kK \, \widehat{p}_{xx} = F(x, t), & x \in (0, c), \, t \in (0, T) \\ \widehat{p}_{x}(0, t) = 0, & t \in (0, T) \\ \widehat{p}_{x}(c, t) = 0, & t \in (0, T) \\ \widehat{p}(x, 0) = \widehat{p}_{0}(x), & x \in (0, c) \end{cases}$$
(117)

36

where

 $F(x,t) = g'(t) + \frac{1}{kab}Q'(t)[x + \frac{1}{2c}(x-c)^2] - \frac{K}{abc}Q(t),$ 

and

$$\widehat{p}_0(x) = p_0(x) + \frac{1}{kab}Q(0)[x + \frac{1}{2c}(x - c)^2].$$

Analytical solution of the 1D-0D coupled problem. Let  $(\cdot, \cdot)_{L^2(0,c)}$  denote the scalar product in the space  $L^2(0,c)$ . Then the solution to (115) is given by

$$p(x,t) = \sum_{0}^{\infty} p_{n} e^{-\frac{n^{2}\pi^{2}}{c^{2}}kKt} \cos\left(\frac{n\pi x}{c}\right) + \sum_{0}^{\infty} \left(\int_{0}^{t} w_{n}(\tau) e^{-\frac{n^{2}\pi^{2}}{c^{2}}kK(t-\tau)} d\tau\right) \cos\left(\frac{n\pi x}{c}\right) - \frac{1}{kab} Q(t) \left[x + \frac{1}{2c}(x-c)^{2}\right]$$
(118)

where

$$\begin{split} p_0 &= \frac{1}{c} \Big( \widehat{p}_0(x), 1 \Big)_{L^2(0,c)} \\ p_n &= \frac{2}{c} \Big( \widehat{p}_0(x), \cos \Big( \frac{n\pi x}{c} \Big) \Big)_{L^2(0,c)}, \quad n \geq 1 \\ w_0(\tau) &= \frac{1}{c} \Big( F(x,\tau), 1 \Big)_{L^2(0,c)}, \quad \tau \in [0,t] \\ w_n(\tau) &= \frac{2}{c} \Big( F(x,\tau), \cos \Big( \frac{n\pi x}{c} \Big) \Big)_{L^2(0,c)}, \quad \tau \in [0,t], \ n \geq 1. \end{split}$$

Now we further simplify the model and assume that the boundary source g = 0, and the initial condition  $\chi = 0$ . Then the solution retains the formula

$$p(x,t) = \sum_{0}^{\infty} p_{n} e^{-\frac{n^{2}\pi^{2}}{c^{2}}kKt} \cos\left(\frac{n\pi x}{c}\right) + \sum_{0}^{\infty} \left(\int_{0}^{t} w_{n}(\tau) e^{-\frac{n^{2}\pi^{2}}{c^{2}}kK(t-\tau)} d\tau\right) \cos\left(\frac{n\pi x}{c}\right) - \frac{1}{kab} Q(t) \left[x + \frac{1}{2c}(x-c)^{2}\right]$$
(119)

with:

$$\begin{split} F(x,t) &= \frac{1}{kab} \mathcal{Q}'(t) \Big[ x + \frac{1}{2c} (x-c)^2 \Big] - \frac{K}{abc} \mathcal{Q}(t) = \frac{1}{2} \frac{\mathcal{Q}'(t)}{kabc} (x^2 + c^2) - \frac{K}{abc} \mathcal{Q}(t) \\ \widehat{p}_0(x) &= \frac{1}{kab} \mathcal{Q}(0) \Big[ x + \frac{1}{2c} (x-c)^2 \Big] = \frac{1}{2} \frac{\mathcal{Q}(0)}{kabc} (x^2 + c^2) \\ p_0 &= \frac{1}{c} \Big( \widehat{p}_0(x), 1 \Big)_{L^2(0,c)} = \frac{2c}{3kab} \cdot \mathcal{Q}(0) \\ p_n &= \frac{2}{c} \Big( \widehat{p}_0(x), \cos \Big( \frac{n\pi x}{c} \Big) \Big)_{L^2(0,c)} = \frac{2(-1)^n}{n^2\pi^2} \cdot \frac{c}{kab} \cdot \mathcal{Q}(0), \quad n \ge 1 \\ w_0(\tau) &= \frac{1}{c} \Big( F(x,\tau), 1 \Big)_{L^2(0,c)} = \frac{2c}{3kab} \cdot \mathcal{Q}'(\tau) - \frac{K}{abc} \mathcal{Q}(\tau), \quad \tau \in [0,t] \\ w_n(\tau) &= \frac{2}{c} \Big( F(x,\tau), \cos \Big( \frac{n\pi x}{c} \Big) \Big)_{L^2(0,c)} = \frac{2(-1)^n}{n^2\pi^2} \cdot \frac{c}{kab} \cdot \mathcal{Q}'(\tau), \quad \tau \in [0,t], \quad n \ge 1 \end{split}$$

From (119), we then recover the pressure P(t) at the Biot-circuit interface as

$$P(t) = p(c,t) = \sum_{n=0}^{\infty} p_n e^{-\frac{n^2 \pi^2}{c^2} kKt} (-1)^n + \int_0^t \sum_{n=0}^{\infty} w_n(\tau) e^{-\frac{n^2 \pi^2}{c^2} kK(t-\tau)} (-1)^n d\tau - \frac{c}{kab} Q(t).$$
 (120)

We recall that, in addition, Q(t) and P(t) must satisfy Poiseuille's law given in (62e), where the pressure  $\pi(t)$  can be computed as  $\pi(t) = \mathbf{y}(t) \cdot \mathbf{e}_1$ ,  $\mathbf{y}(t)$  being given by (63). Overall, equations (120), (62e) and the first component of (63) constitute a system of three nonlinear equations that can be solved to obtain the three unknown functions P(t), Q(t) and  $\pi(t)$ . Lastly, the pressure p(x,t) can be recovered in  $\Omega \times (0,T)$  using formula (119).

**Particular solution of the 1D-0D example**. In order to compare the accuracy of the proposed numerical methods, we consider the particular case in which the flow rate Q(t) at the interface is given by

$$Q(t) = -\widetilde{Q}(1 - e^{-(\alpha t)^s}) \tag{121}$$

where  $\widetilde{Q}$ ,  $\alpha$  and s are positive constants. Then, the pressure P(t) at the interface can be calculated using (120) and the pressure p(x,t) in the whole Biot domain can be calculated using (119). Next, the velocity v(x,t) and the displacement u(x,t) can be obtained as:

$$v(x,t) = -k\frac{\partial p(x,t)}{\partial x} \tag{122}$$

$$u(x,t) = \int_0^t (v(c,s) - v(x,s)) \, ds \,. \tag{123}$$

We notice that the displacement u = u(x, t) can be recovered also through the following alternate expression

$$u(x,t) = \frac{1}{K} \left[ \int_0^x p(\psi,t) \, d\psi - \int_0^c p(\psi,t) \, d\psi \right].$$

Let us now consider the state variables of the lumped circuit. Utilizing expressions (121) and (120) in the Poiseuille law (62e), we can calculate the expression for  $\pi(t)$  as

$$\pi(t) = P(t) - R Q(t). \tag{124}$$

Next, using the circuit state equations and the expressions obtained so far, we can calculate  $Q_1(t)$  and  $\pi_1(t)$  as

$$Q_1(t) = Q(t) - C\frac{d\pi(t)}{dt}$$
(125)

$$\pi_1(t) = \pi - R_1 Q_1(t) - L_1 \frac{dQ_1(t)}{dt}$$
(126)

and we can define the imposed pressure  $\overline{p}(t)$  as

$$\overline{p}(t) = \overline{R} C_1 \frac{d\pi_1(t)}{dt} + \pi_1(t) - \overline{R} Q_1(t).$$
(127)

The particular solution exhibited above satisfies the following initial conditions:

$$u(x,0) = 0$$
 and  $\mathbf{v}(0) = \mathbf{0}$ . (128)

The parameter values summarized in Table 2 are utilized in the numerical simulations reported in Section 8.

Parameter	Description	Value	Unit
а	Domain width	0.1	m
b	Domain height	0.1	m
c	Domain length	0.5	m
$T_{ m end}$	Final time	10	S
k	Permeability	1	$m^4N^{-1}s^{-1}$
K	Aggregate modulus	1	$\mathrm{Nm}^{-2}$
R	Resistance	1	$Nsm^{-5}$
C	Capacitance	$10^{-3}$	$m^5N^{-1}$
$R_1$	Resistance	1	$Nsm^{-5}$
$C_1$	Capacitance	$10^{-1}$	$m^5N^{-1}$
$L_1$	Inductance	1	$Ns^2m^{-5}$
$\overline{R}$	Resistance	1	$Nsm^{-5}$
$\widetilde{Q}$	Parameter in (121)	$10^{-4}$	$m^3s^{-1}$
$\alpha$	Parameter in (121)	$2/T_{\rm end}$	$s^{-1}$
S	Parameter in (121)	4	-

Table 2: Model parameters used in the numerical simulations.

## Appendix II: HDG discretization and its implementation

For the numerical treatment of the three dimensional Biot system, we rewrite it in mixed form:

$$v + \mathbf{K}\nabla p = \mathbf{0},$$

$$\frac{\partial \nabla \cdot \mathbf{u}}{\partial t} + \nabla \cdot \mathbf{v} = S,$$

$$\mathcal{A}\mathbf{T} + P_T p \mathbf{I} - \mathbf{E} = \mathbf{0},$$

$$\nabla \cdot \mathbf{T} + f = \mathbf{0},$$
(129)

where the hydraulic permeability K is a symmetric positive-definite matrix,  $\mathcal{A}$  is the compliance tensor and  $P_T$  $\frac{1}{3\lambda+2\mu}$ . Note that  $\mathcal{A}\mathbf{T} = c_1\mathbf{T} + c_2 \operatorname{tr}(\mathbf{T})\mathbf{I}$ , with

$$c_1 = \frac{1}{2\mu}, \quad c_2 = -\frac{1}{2\mu(2\mu/\lambda + 3)}.$$

On the interface  $\Sigma$  we impose the following conditions:

$$\boldsymbol{u}(\boldsymbol{x},t) = \boldsymbol{0},\tag{130a}$$

$$\int_{\Sigma} v(x,t) \cdot n(x) dx = Q_{\text{target}}(t), \quad p(x,t) = C(t),$$
(130b)

where C(t) is an unknown function that only depends on t.

Let  $\mathcal{T}_h$  denote a conforming triangulation of  $\Omega$  made of shape-regular d-simplices K. We denote by  $\partial \mathcal{T}_h$  the set  $\{\partial K \colon K \in \mathcal{T}_h\}$ . For an element  $K \in \mathcal{T}_h$ ,  $F = \partial K \cap \partial \Omega$  is a boundary face if the d-1 Lebesgue measure of F is nonzero. For two elements  $K^+$  and  $K^-$  of  $\mathcal{T}_h$ ,  $F = \partial K^+ \cap \partial K^-$  is the interior face between  $K^+$  and  $K^-$  if the d-1 Lebesgue measure of F is nonzero. Let  $\mathcal{E}_h^0$  and  $\mathcal{E}_h^{\partial}$  denote the set of interior and boundary faces, respectively. We denote by  $\mathcal{E}_h$  the union of  $\mathcal{E}_h^0$  and  $\mathcal{E}_h^0$ . Assuming that  $\mathcal{T}_h$  is such that for faces  $F \in \mathcal{E}_h^{\partial}$  either  $F \subset \Gamma_{D,v}$ ,  $F \subset \Gamma_{D,p}$ ,  $F \subset \Gamma_N$ ,  $F \subset \Gamma_0$  or  $F \subset \Sigma$ , the sets of boundary faces can be further split into the subsets  $\mathcal{E}_h^{\Gamma_{D,v}}$ ,  $\mathcal{E}_h^{\Gamma_D,p}$ ,  $\mathcal{E}_h^{\Gamma_D}$ , and  $\mathcal{E}_h^{\Gamma}$ . Let  $\mathcal{P}_k(D)$  denote the set of polynomials of degree at most k on a domain D. Also, if S(D) denotes a space of

scalar-valued functions defined on D, the corresponding space of vector-valued functions is  $S(D) = (S(D))^d$  and

the corresponding space of matrix-valued functions is  $S(D) = (S(D))^{d \times d}$ . Finally,  $S(D)_{\text{sym}}$  denotes the symmetric subspace of S(D). We are going to use the following discontinuous finite element spaces:

$$\begin{split} \mathbf{V}_{h}^{u} &= \left\{ \tau \in \mathbf{L}^{2}(\Omega)_{\text{sym}} \mid \tau|_{K} \in \mathcal{P}_{k}(K)_{\text{sym}} \quad \forall K \in \mathcal{T}_{h} \right\}, \\ \mathbf{W}_{h}^{u} &= \left\{ \mathbf{w} \in \mathbf{L}^{2}(\Omega) \mid \mathbf{w}|_{K} \in \mathcal{P}_{k+1}(K) \quad \forall K \in \mathcal{T}_{h} \right\}, \\ \mathbf{M}_{h}^{u} &= \left\{ \mathbf{\mu} \in \mathbf{L}^{2}(\mathcal{E}_{h}) \mid \boldsymbol{\mu}|_{F} \in \mathcal{P}_{k}(F) \quad \forall F \in \mathcal{E}_{h} \right\}, \\ \mathbf{V}_{h}^{p} &= \left\{ \mathbf{r} \in \mathbf{L}^{2}(\Omega) \mid \mathbf{r}|_{K} \in \mathcal{P}_{k}(K) \quad \forall K \in \mathcal{T}_{h} \right\}, \\ \mathbf{W}_{h}^{p} &= \left\{ \mathbf{q} \in \mathbf{L}^{2}(\Omega) \mid \mathbf{q}|_{K} \in \mathcal{P}_{k^{*}}(K) \quad \forall K \in \mathcal{T}_{h} \right\}, \\ \widetilde{\mathbf{M}}_{h}^{p} &= \left\{ \mathbf{q} \in \mathbf{L}^{2}(\mathcal{E}_{h}) \mid \boldsymbol{\eta}|_{F} \in \mathcal{P}_{k}(F) \\ \forall F \in \mathcal{E}_{h}^{0} \cup \mathcal{E}_{h}^{\Gamma_{D,p}} \cup \mathcal{E}_{h}^{\Gamma_{N}} \cup \mathcal{E}_{h}^{\Gamma_{0}}, \ \boldsymbol{\eta}|_{\Sigma} = 0 \right\}, \\ \mathbf{M}_{h}^{*,p} &= \left\{ \mathbf{q} \in \mathbf{L}^{2}(\mathcal{E}_{h}) \mid \boldsymbol{\eta}|_{\Sigma} = \alpha, \alpha \in \mathbb{R}, \ \boldsymbol{\eta}|_{\mathcal{E}_{h} \setminus \Sigma} = 0 \right\}, \\ \mathbf{M}_{h}^{p,1} &= \widetilde{\mathbf{M}}_{h}^{p} \oplus \mathbf{M}_{h}^{*,p}, \\ \mathbf{M}_{h}^{p,2} &= \left\{ \boldsymbol{\eta} \in \mathbf{L}^{2}(\mathcal{E}_{h}) \mid \boldsymbol{\eta}|_{F} \in \mathcal{P}_{k}(F) \quad \forall F \in \mathcal{E}_{h} \right\}, \end{split}$$

where  $k^* \in \{k, k+1\}$ . For functions  $\mathbf{w}, \mathbf{v}$  in  $\mathbf{L}^2(D)$ , we denote  $(\mathbf{w}, \mathbf{v})_D = \sum_{i=1, j=1}^d \int_D w_{ij} v_{ij}$ . For functions  $\mathbf{w}, \mathbf{v}$  in  $\mathbf{L}^2(D)$ , we denote  $(\mathbf{w}, \mathbf{v})_D = \int_D \mathbf{w} \cdot \mathbf{v}$  if  $D \subset \mathbb{R}^d$  and  $\langle \mathbf{w}, \mathbf{v} \rangle_D = \int_D \mathbf{w} \cdot \mathbf{v}$  if  $D \subset \mathbb{R}^{d-1}$ . For functions  $\mathbf{w}, \mathbf{v}$  in  $L^2(D)$ , we denote  $(\mathbf{w}, \mathbf{v})_D = \int_D \mathbf{w} \mathbf{v}$  if  $D \subset \mathbb{R}^d$  and  $\langle \mathbf{w}, \mathbf{v} \rangle_D = \int_D \mathbf{w} \mathbf{v}$  if  $D \subset \mathbb{R}^{d-1}$ . We then introduce

$$(w,v)_{\mathcal{T}_h} = \sum_{K \in \mathcal{T}_h} (w,v)_K, \qquad \langle \mu, \eta \rangle_{\partial \mathcal{T}_h} = \sum_{K \in \mathcal{T}_h} \langle \mu, \eta \rangle_{\partial K},$$

for w, v defined on  $\mathcal{T}_h$  and  $\mu, \eta$  defined on  $\partial \mathcal{T}_h$ . In analogy with [69], we define the scaled velocity  $\tilde{\mathbf{v}} = \mathbf{K}^{-1/2}\mathbf{v}$ . This choice allows a better control of the gradient of the fluid pressure. A more detailed explanation is outside the scope of the current work, but can be provided using similar arguments as in [69]. The HDG method for the Biot system (129) using the scaled velocity, equipped with the given boundary conditions, and using the backward Euler method for temporal discretization, seeks to define  $(\mathbf{T}_h^{n+1}, u_h^{n+1}, \hat{u}_h^{n+1}, \hat{v}_h^{n+1}, p_h^{n+1}, \hat{p}_h^{n+1}) \in \mathbf{V}_h^u \times \mathbf{W}_h^u \times \mathbf{W}_h^u \times \mathbf{W}_h^v \times \mathbf{W}_h^p \times \mathbf{W}_h^{p,1}$  at time step n+1 as the solution of the following system [70, 66]:

$$(\tilde{\boldsymbol{v}}_{h}^{n+1}, \boldsymbol{r})_{\mathcal{T}_{h}} + \langle (\mathbf{K}^{n+1})^{1/2} \boldsymbol{r} \cdot \boldsymbol{n}, \hat{p}_{h}^{n+1} \rangle_{\partial \mathcal{T}_{h}} - (p_{h}^{n+1}, \nabla \cdot ((\mathbf{K}^{n+1})^{1/2} \boldsymbol{r}))_{\mathcal{T}_{h}} = 0,$$

$$\frac{1}{\Delta t} (\nabla \cdot \boldsymbol{u}_{h}^{n+1}, q)_{\mathcal{T}_{h}} + \langle \hat{\boldsymbol{v}}_{h}^{n+1} \cdot \boldsymbol{n}, q \rangle_{\partial \mathcal{T}_{h}} - ((\mathbf{K}^{n+1})^{1/2} \tilde{\boldsymbol{v}}_{h}^{n+1}, \nabla q)_{\mathcal{T}_{h}} =$$

$$(131a)$$

$$\frac{1}{\Delta t} (\nabla \cdot \boldsymbol{u}_{h}^{n}, q)_{\mathcal{T}_{h}} + (S^{n+1}, q)_{\mathcal{T}_{h}}, \tag{131b}$$

$$c_1(\mathbf{T}_n^{n+1}, \tau)_{\mathcal{T}_h} + c_2(\operatorname{tr}(\mathbf{T}_h^{n+1}), \operatorname{tr}(\tau))_{\mathcal{T}_h} + (\boldsymbol{u}_h^{n+1}, \nabla \cdot \tau)_{\mathcal{T}_h} - \langle \tau \boldsymbol{n}, \hat{\boldsymbol{u}}_h^{n+1} \rangle_{\partial \mathcal{T}_h}$$

$$+P_T(p_h^{n+1}, \text{tr}(\tau))_{\mathcal{T}_h} = 0,$$
 (131c)

$$\langle \mathbf{\hat{T}}_h^{n+1} \mathbf{n}, \mathbf{w} \rangle_{\partial \mathcal{T}_h} - (\mathbf{T}_h^{n+1}, \nabla \mathbf{w})_{\mathcal{T}_h} + (\mathbf{f}^{n+1}, \mathbf{w})_{\mathcal{T}_h} = 0, \tag{131d}$$

$$\langle \hat{\boldsymbol{v}}_h^{n+1} \cdot \boldsymbol{n}, \boldsymbol{\eta} \rangle_{\partial \mathcal{T}_h \setminus \partial \Omega} + \langle \hat{\boldsymbol{v}}_h^{n+1} \cdot \boldsymbol{n}, \boldsymbol{\eta} \rangle_{\Gamma_{D,v}} + \langle \hat{\boldsymbol{v}}_h^{n+1} \cdot \boldsymbol{n}, \boldsymbol{\eta} \rangle_{\Sigma} =$$

$$\langle \psi^{n+1}, \eta \rangle_{\Gamma_{D,\nu}} + Q_{\text{target}}^{n+1} |\Sigma|^{-1} \langle \mu, 1 \rangle_{\Sigma},$$
 (131e)

$$\langle \hat{p}_h^{n+1}, \eta \rangle_{\Gamma_{D,p}} = 0, \qquad \hat{p}_h^{n+1}|_{\Sigma} = \text{unknown constant},$$
 (131f)

$$\langle \hat{\mathbf{T}}_{h}^{n+1} \mathbf{n}, \boldsymbol{\mu} \rangle_{\partial \mathcal{T}_{h} \setminus \partial \Omega} + \langle \hat{\mathbf{T}}_{h}^{n+1} \mathbf{n}, \boldsymbol{\mu} \rangle_{\Gamma_{N}} = \langle \mathbf{g}^{n+1}, \boldsymbol{\mu} \rangle_{\Gamma_{N}}$$
(131g)

$$\langle \hat{\boldsymbol{u}}_{h}^{n+1}, \boldsymbol{\mu} \rangle_{\Gamma_{D,p} \cup \Gamma_{D,v} \cup \Sigma} = 0 \qquad \langle \hat{\boldsymbol{u}}_{h}^{n+1} \cdot \boldsymbol{n}, \boldsymbol{\mu} \cdot \boldsymbol{n} \rangle_{\Gamma_{0}} = 0, \tag{131h}$$

for all  $\mathbf{V}_h^u \times \mathbf{W}_h^u \times \mathbf{M}_h^u \times \mathbf{V}_h^p \times \mathbf{W}_h^p \times \mathbf{M}_h^{p,1}$ , where:

$$\mathbf{\hat{T}}_{h}^{n+1} \mathbf{n} = \mathbf{T}_{h}^{n+1} \mathbf{n} - \tau_{S} (P_{M^{u}} \mathbf{u} - \hat{\mathbf{u}}_{h}^{n+1}) \quad \text{on } \partial \mathcal{T}_{h}, \tag{132a}$$

$$\hat{\mathbf{v}}_{h}^{n+1} \cdot \mathbf{n} = (\mathbf{K}^{n+1})^{1/2} \tilde{\mathbf{v}}_{h}^{n+1} \cdot \mathbf{n} + \tau_{F} (P_{M^{p}} p_{h}^{n+1} - \hat{p}_{h}^{n+1}) \quad \text{on } \partial \mathcal{T}_{h}.$$
(132b)

The operator  $P_{M^u}(P_{M^p})$  denotes the standard  $L^2$ -orthogonal projection from  $L^2(\mathcal{E}_h)$  ( $L^2(\mathcal{E}_h)$ ) onto  $M_h^u(M_h^{p,1})$ . Also,  $|\Sigma|$  denotes the d-1 Lebesgue measure of  $\Sigma$ .

Here  $(\mathbf{T}_h^{n+1}, \boldsymbol{u}_h^{n+1}, \hat{\boldsymbol{u}}_h^{n+1}, \hat{\boldsymbol{v}}_h^{n+1}, p_h^{n+1}, \hat{p}_h^{n+1})$  represents the numerical approximation to the exact solution  $(\mathbf{T}, \boldsymbol{u}, \boldsymbol{u}|_{\mathcal{E}_h}, \tilde{\boldsymbol{v}}, p, p|_{\mathcal{E}_h})$  at time  $t^{n+1}$ . We could prove that  $\hat{p}_h^{n+1}|_{\Sigma}$  is the Lagrange multiplier associated with the integral boundary condition embedded in (131e), thereby implying the condition on the right hand side of (131f) [66].

**Implementation in the PQP subiterations.** In Step 1 of the PQP subiterations,  $\hat{p}_h^{n+1}$  and the test function  $\eta$  are taken in the space  $M_h^{p,2}$  rather than  $M_h^{p,1}$ . Also, the IBC (130b) is replaced by  $p(\mathbf{x}, t^{n+1}) = P_{(j)}$  on  $\Sigma \times (t^n, t^{n+1})$ , so that equations (131e) and (131f) become, respectively:

$$\langle \hat{\boldsymbol{v}}_{h}^{n+1} \cdot \boldsymbol{n}, \eta \rangle_{\partial \mathcal{T}_{h} \setminus \partial \Omega} + \langle \hat{\boldsymbol{v}}_{h}^{n+1} \cdot \boldsymbol{n}, \eta \rangle_{\Gamma_{D,v}} = \langle \psi^{n+1}, \eta \rangle_{\Gamma_{D,v}},$$

$$\langle \hat{\boldsymbol{p}}_{h}^{n+1}, \eta \rangle_{\Gamma_{D,p}} = 0, \qquad \langle \hat{\boldsymbol{p}}_{h}^{n+1}, \eta \rangle_{\Sigma} = P_{(j)},$$

for all  $\eta \in M_h^{p,2}$ .

**Implementation in the QPQ subiterations.** The problem we have to solve in Step 1 of the QPQ subiterations is identical to (131), provided that we take  $Q_{\text{target}}^{n+1} = Q_{(j)}$ .

**Implementation in then operator splitting method.** In Step 1 of the operator splitting method, we have to solve a system analogous to (131), provided that the we impose an appropriate IBC on  $\Sigma$ . The interface conditions on  $\Sigma$  discretized by the backward Euler method read

$$\langle \hat{\mathbf{v}}_{h}^{n+1} \cdot \mathbf{n}, \eta \rangle_{\Sigma} = Q^{n+1}, \quad \hat{p}_{h}^{n+1} = P^{n+1}, \quad Q^{n+1} = \frac{P^{n+1} - \pi^{n+1}}{R}.$$
 (133)

Moreover, the simple circuit to be solved in Step 1 is equivalent to the scalar ODE  $\frac{d\pi}{dt} = \frac{Q(t)}{C}$ , which is discretized as follows

$$\frac{\pi^{n+1} - \pi^n}{\Lambda t} = \frac{Q^{n+1}}{C}. (134)$$

By combining (134) with the rightmost equation of (133), we get

$$\pi^{n+1} = \frac{\Delta t}{RC + \Delta t} P^{n+1} + \frac{RC}{RC + \Delta t} \pi^n, \tag{135}$$

which can be combined with the leftmost equation of (133) to obtain

$$\langle \hat{\mathbf{v}}_{h}^{n+1} \cdot \mathbf{n}, \eta \rangle_{\Sigma} = Q^{n+1} = \frac{P^{n+1} - \pi^{n+1}}{R} = \frac{C}{RC + \Delta t} (P^{n+1} - \pi^{n}). \tag{136}$$

The last equation is ready to be used in the HDG discretization (131). In particular, after recasting the system (131) in terms of a global linear system for the unknowns  $\hat{u}_h^{n+1}$ ,  $\hat{p}_h^{n+1}$  by using a static condensation approach and by observing that  $\hat{p}_h^{n+1}|_{\Sigma} = P^{n+1}$ , the IBC (136) resorts to adding the value  $-\frac{C}{RC+\Delta t}\pi^n$  to the global right hand side in the degree of freedom corresponding to  $\hat{p}_h^{n+1}|_{\Sigma}$ , say i, and adding  $-\frac{C}{RC+\Delta t}$  to the (i,i)-th element of the global matrix. After solving the linear system and retrieving the value of  $\hat{p}_h^{n+1}|_{\Sigma}$ , equation (135) can be used to compute  $\pi^{n+1}$ , which is then used to update the initial condition for Step 2.

#### References

- [1] B. M. L. Baffico, C. Grandmont, Multiscale modeling of the respiratory tract, Mathematical Models and Methods in Applied Sciences 20 (2010) 59–93.
- [2] S. M. J. Fouchet-Incaux, C. Grandmont, Numerical stability of coupling schemes in the 3d/0d modelling of airflows and blood flows, 2014. Preprint available at https://hal/inria/fr/hal-01095960/document, 29pp., 2014.
- [3] T. Gengenbach, V. Heuveline, M. J. Krause, Numerical simulation of the human lung: A two-scale approach, 2011. Karlsruhe Institute of Technology (KIT), Engineering Mathematics and Computing Lab (EMCL), Preprint Series, 11, 2011.
- [4] C. Grandmont, Y. Maday, B. Maury, A multiscale/multimodel approach of the respiration tree. New Trends in Continuum Mechanics, 2005. Theta Series in Advanced Mathematics (Bucharest), volume 3 (2005), 147-157.
- [5] M. Ismail, A. Comerford, W. Wall, Coupled and reduced dimensional modeling of respiratory mechanics during spontaneous breathing, International Journal for Numerical Methods in Biomedical Engineering 29 (2013) 1285–1305.

- [6] A. P. Kuprat, S. Kabilan, J. P. Carson, R. A. Corley, D. R. Einstein, A bidirectional coupling procedure applied to multiscale respiratory modeling, Journal of Computational Physics 244 (2013) 148–167.
- [7] B. Maury, The Respiratory System in Equations, 2013. Modeling, Simulation and Applications. Volume 7. Springer-Verlag Italia, Milan, 2013
- [8] M. E. Moghadam, I. E. Vignon-Clementel, R. Figliola, A. L. Marsden, A modular numerical method for implicit 0d/3d coupling in cardio-vascular finite element simulations, Journal of Computational Physics 244 (2013) 63–79.
- [9] A. Quarteroni, S. Ragni, A. Veneziani, Coupling between lumped and distributed models for blood flow problems, Computing and Visualization in Science 4 (2001) 111–124.
- [10] A. Quarteroni, A. Veneziani, Analysis of a geometrical multiscale model based on the coupling of ode and pde for blood flow simulations, Multiscale Modeling & Simulation 1 (2003) 173–195.
- [11] M. Á. Fernández, V. Milisic, A. Quarteroni, Analysis of a geometrical multiscale blood flow model based on the coupling of odes and hyperbolic pdes, Multiscale Modeling & Simulation 4 (2005) 215–236.
- [12] L. Formaggia, A. Quarteroni, A. Veneziani, Cardiovascular Mathematics: Modeling and simulation of the circulatory system, volume 1, Springer-Verlag Mailand, 2009.
- [13] R. Torii, M. Oshima, T. Kobayashi, K. Takagi, T. E. Tezduyar, Coupling 3d fluid-structure interaction modeling of cerebral aneurysm with 0d arterial network model as boundary conditions, Transaction of the Japan Society for Simulation Technology 1 (2009) 81–90.
- [14] A. Quarteroni, A. Veneziani, C. Vergara, Geometric multiscale modeling of the cardiovascular system, between theory and practice, Computer Methods in Applied Mechanics and Engineering 302 (2016) 193–252.
- [15] L. Carichino, G. Guidoboni, M. Szopos, Energy-based operator splitting approach for the time discretization of coupled systems of partial and ordinary differential equations for fluid flows: The stokes case, Journal of Computational Physics 364 (2018) 235–256.
- [16] L. Carichino, G. Guidoboni, M. Szopos, An operator splitting approach for the time discretization of coupled systems of partial and ordinary differential equations for fluid flows, 2020. Numerical Mathematics and Advanced Applications (ENUMATH 2019). Accepted. In Press.
- [17] I. G. Gjerde, K. Kumar, J. M. Nordbotten, A singularity removal method for coupled 1d-3d flow models, Computational Geosciences 24 (2020) 443-457.
- [18] R. Al-Khoury, P. G. Bonnier, R. B. J. Brinkgreve, Efficient finite element formulation for geothermal heating systems. part i: steady state, International Journal for Numerical Methods in Engineering 63 (2005) 988–1013.
- [19] L. Cattaneo, P. Zunino, A computational model of drug delivery through microcirculation to compare different tumor treatments, International Journal for Numerical Methods in Biomedical Engineering 30 (2014) 1347–1371.
- [20] L. Grinberg, E. Cheever, T. Anor, J. R. Madsen, G. E. Karniadakis, Modeling blood flow circulation in intracranial arterial networks: A comparative 3d/1d simulation study, Annals of Biomedical Engineering 39 (2011) 297–309.
- [21] M. Nabil, P. Zunino, A computational study of cancer hyperthermia based on vascular magnetic nanoconstructs, Royal Society Open Science 3 (2016).
- [22] L. Possenti, G. Casagrande, S. Di Gregorio, P. Zunino, M. L. Costantino, Numerical simulations of the microvascular fluid balance with a non-linear model of the lymphatic system, Microvascular Research 122 (2019) 101–110.
- [23] J. Reichold, M. Stampanoni, A. L. Keller, A. Buck, P. Jenny, B. Weber, Vascular graph model to simulate the cerebral blood flow in realistic vascular networks, Journal of Cerebral Blood Flow & Metabolism 29 (2009) 1429–1443.
- [24] R. Sacco, G. Guidoboni, A. G. Mauri, A Comprehensive Physically Based Approach to Modeling in Bioengineering and Life Sciences, Elsevier, Cambridge MA 02139, USA, 2019. 1st Edition.
- [25] A.-R. Khaled, K. Vafai, The role of porous media in modeling flow and heat transfer in biological tissues, International Journal of Heat and Mass Transfer 46 (2003) 4989–5003.
- [26] P. Causin, G. Guidoboni, A. Harris, D. Prada, R. Sacco, S. Terragni, A poroelastic model for the perfusion of the lamina cribrosa in the optic nerve head, Mathematical Biosciences 257 (2014) 33–41.
- [27] D. Chapelle, J.-F. Gerbeau, J. Sainte-Marie, I. Vignon-Clementel, A poroelastic model valid in large strains with applications to perfusion in cardiac modeling, Computational Mechanics 46 (2010) 91–101.
- [28] M. Verri, G. Guidoboni, L. Bociu, R. Sacco, The role of structural viscoelasticity in deformable porous media with incompressible constituents: Applications in biomechanics, Mathematical Biosciences & Engineering 15 (2018) 933–959.
- [29] L. Bociu, G. Guidoboni, R. Sacco, M. Verri, On the role of compressibility in poroviscoelastic models, Mathematical Biosciences and Engineering 16 (2019) 6167–6208.
- [30] M. Bukac, W. Layton, M. Moraiti, H. Tran, C. Trenchea, Analysis of partitioned methods for the biot system, Numerical Methods for Partial Differential Equations 31 (2015) 1769–1813.
- [31] L. Bociu, G. Guidoboni, R. Sacco, J. Webster, Analysis of nonlinear poro-elastic and poro-visco-elastic models, Archive for Rational Mechanics and Analysis 222 (2016) 1445–1519.
- [32] M. K. Brun, E. Ahmed, J. M. Nordbotten, F. A. Radu, Well-posedness of the fully coupled quasi-static thermo-poroelastic equations with nonlinear convective transport, Journal of Mathematical Analysis and Applications 471 (2019) 239–266.
- [33] L. D. O. Vilaca, B. Gómez-Vargas, S. Kumar, R. Ruiz-Baier, N. Verma, Stability analysis for a new model of multi-species convection-diffusion-reaction in poroelastic tissue, Applied Mathematical Modelling 84 (2020) 425–446.
- [34] M. A. Biot, General theory of three-dimensional consolidation, Journal of Applied Physics 12 (1941) 155–164.
- [35] L. Formaggia, F. Nobile, A. Quarteroni, A. Veneziani, Multiscale modelling of the circulatory system: a preliminary analysis, Comput Visual Sci 2 (1999) 75–83.
- [36] Milisi'c, Vuk, Quarteroni, Alfio, Analysis of lumped parameter models for blood flow simulations and their relation with 1d models, ESAIM:M2AN 38 (2004) 613–632.
- [37] O. Coussy, Poromechanics, Wiley, New York, 02004.
- [38] R. de Boer, Trends in Continuum Mechanics of Porous Media, Theory and Applications of Transport in Porous Media, Springer Netherlands, 2006. URL: https://books.google.it/books?id=PIq3tg5rBvQC.
- [39] S. M. Klisch, R. L. Sah, A. Hoger, A cartilage growth mixture model for infinitesimal strains: solutions of boundary-value problems related to in vitro growth experiments, Biomech Model Mechanobiol 3 (2005) 209–223.
- [40] G. Ateshian, R. Nims, S. Maas, J. Weiss, Computational modeling of chemical reactions and interstitial growth and remodeling involving

- charged solutes and solid-bound molecules, Biomech Model Mechanobiol 13 (2014) 1105-1120.
- [41] S. BG, O. CWJ, B. FPT, An integrated finite-element approach to mechanics, transport and biosynthesis in tissue engineering, J Biomech Eng 126 (2004) 82–91.
- [42] R. Sacco, P. Causin, C. Lelli, M. T. Raimondi, A poroelastic mixture model of mechanobiological processes in biomass growth: theory and application to tissue engineering, Meccanica 52 (2017) 3273–3297.
- [43] A. J. Grodzinsky, Electromechanical and physicochemical properties of connective tissue, Crit Rev Biomed Eng. 9 (1983) 133–199.
- [44] A. J. H. Frijns, A four-component mixture theory applied to cartilaginous tissues: numerical modelling and experiments, Ph.D. thesis, Technische Universiteit Eindhoven, 2000. Https://doi.org/10.6100/IR537990.
- [45] R. de Boer, Theory of Porous Media, Springer Berlin Heidelberg, 2000.
- [46] M. H. Friedman, Principles and Models of Biological Transport, Springer New York, 2008.
- [47] C. Desoer, E. Kuh, Basic circuit theory, McGraw Hill international editions: Electrical and Electronic Engineering Series, McGraw-Hill, 1969
- [48] J.-L. Auriault, E. Sanchez-Palencia, A study of the macroscopic behavior of a deformable saturated porous medium, Journal de Mecanique 10 (1977) 575–603.
- [49] A. Zenisek, The existence and uniqueness theorem in biot's consolidation theory, Appl. Math. 29 (1984) 194–211.
- [50] R. Showalter, Diffusion in poro-elastic media, JMAA 251 (2000) 310-340.
- [51] N. Su, R. Showalter, Partially saturated flow in a poroelastic medium, DCDS-B 1 (2001) 403-420.
- [52] Y. Cao, S. Chen, A. Meir, Analysis and numerical approximations of equations of nonlinear poroelasticity, DCDS-B 18 (2013) 1253–1273.
- [53] L. Bociu, J. Webster, Nonlinear quasi-static poroelasticity, Journal of Differential Equations 296 (2021) 242–278.
- [54] L. Bociu, B. Muha, J. Webster, Weak solutions in nonlinear poroelasticity with incompressible constituents, Nonlinear Analysis: Real World Applications 67 (2022).
- [55] E. H. Zarantonello, Solving Functional Equations by Contractive Averaging, MRC technical summary report: Mathematics Research Center, Mathematics Research Center, United States Army, University of Wisconsin, 1960.
- [56] A. Quarteroni, A. Valli, Domain decomposition methods for partial differential equations, Numerical Mathematics Scientific Computation, Clarendon Press, 1999.
- [57] R. Glowinski, S. J. Osher, W. Yin, Splitting methods in Communication, Imaging, Science, and Engineering, Springer, 2017.
- [58] G. Marchuk, Splitting and alternating direction methods, Handbook of Numerical Analysis 1 (1990) 197-462.
- [59] R. Glowinski, Numerical methods for fluids (part 3), Handbook of Numerical Analysis 9 (2003).
- [60] R. Glowinski, G. Guidoboni, T.-W. Pan, Wall-driven incompressible viscous flow in a two-dimensional semi-circular cavity, Journal of Computational Physics 216 (2006) 76–91.
- [61] R. Glowinski, E. Dean, G. Guidoboni, H. Juarez, T.-W. Pan, Applications of operator-splitting methods to the direct simulation of particulate and free-surface flows and to the numerical solution of the two-dimensional elliptic monge-ampere equation, Japan Journal of Industrial and Applied Mathematics 25 (2008) 1–63.
- [62] G. Guidoboni, R. Glowinski, N. Cavallini, S. Canic, Stable loosely-coupled-type algorithm for fluid-structure interaction in blood flow, Journal of Computational Physics 228 (2009) 6916–6937.
- [63] L. Carichino, G. Guidoboni, M. Szopos, Energy-based operator splitting approach for the time discretization of coupled systems of partial and ordinary differential equations for fluid flows: The stokes case, Journal of Computational Physics 364 (2018) 235–256.
- [64] J. Ortega, W. Rheinboldt, Iterative Solution of Nonlinear Equations in Several Variables, Academic Press, New York, 1970.
- [65] E. Zeidler, Vol I: Fixed point theorems, Nonlinear Functional Analysis and Its Applications, Springer-Verlag, 1986.
- [66] S. Bertoluzza, G. Guidoboni, R. Hild, D. Prada, C. Prud'homme, R. Sacco, L. Sala, M. Szopos, A hdg method for elliptic problems with integral boundary condition, 2022. Manuscript submitted for publication.
- [67] M.-D. Huang, The constant-flow patch test a unique guideline for the evaluation of discretization schemes for the current continuity equations, IEEE Transactions on Computer-Aided Design of Integrated Circuits and Systems 4 (1985) 583–608.
- [68] O. Zienkiewicz, R. Taylor, The finite element patch test revisited a computer test for convergence, validation and error estimates, Computer Methods in Applied Mechanics and Engineering 149 (1997) 223–254. Containing papers presented at the Symposium on Advances in Computational Mechanics.
- [69] S. Kang, T. Bui-Thanh, T. Arbogast, A hybridized discontinuous galerkin method for a linear degenerate elliptic equation arising from two-phase mixtures, Computer Methods in Applied Mechanics and Engineering 350 (2019) 315–336.
- [70] D. Prada, A hybridizable discontinuous Galerkin method for nonlinear porous media viscoelasticity with applications in ophthalmology, Ph.D. thesis, Indiana University Purdue University Indianapolis, 2016.